



저작자표시-비영리-변경금지 2.0 대한민국

이용자는 아래의 조건을 따르는 경우에 한하여 자유롭게

- 이 저작물을 복제, 배포, 전송, 전시, 공연 및 방송할 수 있습니다.

다음과 같은 조건을 따라야 합니다:



저작자표시. 귀하는 원저작자를 표시하여야 합니다.



비영리. 귀하는 이 저작물을 영리 목적으로 이용할 수 없습니다.



변경금지. 귀하는 이 저작물을 개작, 변형 또는 가공할 수 없습니다.

- 귀하는, 이 저작물의 재이용이나 배포의 경우, 이 저작물에 적용된 이용허락조건을 명확하게 나타내어야 합니다.
- 저작권자로부터 별도의 허가를 받으면 이러한 조건들은 적용되지 않습니다.

저작권법에 따른 이용자의 권리는 위의 내용에 의하여 영향을 받지 않습니다.

이것은 [이용허락규약\(Legal Code\)](#)을 이해하기 쉽게 요약한 것입니다.

[Disclaimer](#)

**Master's Thesis of Engineering**

**Modulation and Regression based  
Hybrid Thermal Sharpening of  
Landsat-8 TIRS Imagery Using  
Fractional Urban Cover**

**도심 피복 비율과 변조 및 회귀 기반의  
하이브리드 열영상 융합 기법을 통한 Landsat-8  
TIRS 영상의 공간해상도 향상**

**August 2019**

**Department of Civil and Environmental  
Engineering  
Seoul National University**

**Kangjoon Cho**

# Modulation and Regression based Hybrid Thermal Sharpening of Landsat-8 TIRS Imagery Using Fractional Urban Cover

지도교수 김 용 일

이 논문을 공학석사 학위논문으로 제출함  
2019년 5월

서울대학교 대학원  
건설환경공학부  
조 강 준

조강준의 공학석사 학위논문을 인준함  
2019년 7월

위 원 장 유 기 운 (인)

부위원장 김 용 일 (인)

위 원 이 창 노 (인)

## Abstract

# Modulation and Regression based Hybrid Thermal Sharpening of Landsat-8 TIRS Imagery Using Fractional Urban Cover

Kangjoon Cho

Department of Civil and Environmental Engineering

The Graduate School

Seoul National University

Thermal data produced from remotely sensed data are significant parameters for investigating biophysical phenomena. However, the spatial resolution of TIR sensors is consequently constrained by the trade-off between spatial and spectral resolutions in Thermal InfraRed (TIR) remote sensing systems. Notable applications of thermal data include wildfires, volcanic activity, and land cover classification, but usage of remotely sensed data are limited to medium-resolution sensors such as Landsat-8 or Advanced Spaceborne Thermal Emission and reflection Radiometer (ASTER) products.

In order to address this problem, various thermal sharpening methods of TIR data based on the Vegetation Index (VI), such as Normalized Different Vegetation Index (NDVI) and Fractional Vegetation Cover (FVC), have been developed to sharpen the coarser spatial resolution of TIR data. Although these methods exhibited a sufficient level of effectiveness, preservation of spatial details in the original TIR data still proved to be difficult, especially in urban areas due to the presence of heterogeneous land cover patterns.

This study has improved the conventional thermal sharpening algorithm by modifying the input index and sharpening model. First, a novel index referred to as Fractional Urban Cover (FUC) is proposed for the thermal sharpening algorithm for Landsat-8 Thermal Infrared Sensor (TIRS). The FUC index is based on Visible Infrared Imaging Radiometer Suite (VIIRS) Day/Night Band (DNB) Night-Time Light (NTL) imagery. Second, to minimize the distortion of spectral features, a Modulation and Regression based Hybrid Thermal Sharpening (MRHTS) model, combined Least Square Regression (LSR) analysis and High Pass Modulation (HPM) were applied for Landsat-8 TIRS imagery. The proposed image sharpening algorithm using the MRHTS framework with the FUC index as its input is abbreviated as MRHTS-FUC.

The MRHTS-FUC algorithm was applied to Landsat-8 Operational Land Imager (OLI), TIRS and VIIRS NTL images in the urban area. The proposed algorithm was compared with algorithms based on the Regression-based Thermal Sharpening

(RTS) model and input variables: RTS-NDVI (DisTrad), RTS-FVC (TsHARP), RTS-FUC, MRHTS-NDVI, and MRHTS-FVC. Quantitative evaluation of the resulting sharpened images was conducted in terms of the synthesis and consistency properties.

Regarding the synthesis property, Structural SIMilarity (SSIM) and Universal Image Quality Index (UIQI) yielded the highest values for the proposed method with values of 0.8013 and 0.8356, respectively. These results indicate that the proposed MRHTS framework effectively reflected the spatial details of the thermal imagery from the FUC index in this study. Regarding the consistency property, the proposed MRHTS framework returned better results over the RTS framework with respect to all of the image quality indices. In addition, visual analysis of the results revealed that the proposed algorithm successfully extracted spatial detail not only in vegetation areas but also in urban land cover, while preserving the spectral information.

The experimental results demonstrated that the proposed algorithm was successfully applied to the TIR data, particularly in urban areas through quantitative and visual assessments. As an extension to the results from this study, urban morphology analysis of biotope and settlement structures can be conducted by enhancing the 100-m spatial resolution of Landsat TIR images to match the finer 30-m resolution of multispectral sensors.

Keywords : Thermal Sharpening, Landsat-8 Thermal InfraRed Sensor (TIRS), Night-Time Light (NTL), Fractional Urban Cover (FUC), Modulation and Regression based Hybrid Thermal Sharpening (MRHTS), Urban areas

*Student Number* : 2017-23626

# Table of Contents

1. Introduction .....	1
1.1 Necessity for Thermal Sharpening .....	1
1.2 Scale Dependency of Urban Remote Sensing .....	5
1.3 Related Works .....	7
1.4 Objective of the Study .....	10
2. Frameworks of Thermal Sharpening and Pansharpening .....	12
2.1 Thermal Sharpening Framework .....	12
2.1.1. Disaggregation of Radiometric Temperature (DisTrad) .....	14
2.1.2. Temperature Sharpening (TsHARP) .....	15
2.2 Pansharpening Framework .....	16
2.2.1. General Pansharpening Approach .....	16
2.2.2. High Pass Modulation (HPM) Method .....	18
3. Input Variable Selection for Thermal Sharpening in Urban Areas .....	19
3.1 Human Settlement Index (HSI) from VIIRS NTL ...	19
3.2 Statistical Analysis between BT and Input Indices	21
3.3 Suggestion of a New Index : Fractional Urban Cover (FUC) .....	24

4. Modulation and Regression based Hybrid Thermal Sharpening Using FUC Index .....	26
4.1 Workflow .....	26
4.2 Preprocessing .....	29
4.3 First Step : Intensity Generation Using Statistical Regression between FUC and BT .....	31
4.4 Second Step : Application of HPM Sharpening .....	32
5. Experimental Design .....	33
5.1 Study Area and Materials .....	33
5.2 Algorithm Selection for Comparison Analysis .....	35
5.3 Image Quality Assessment .....	37
5.3.1. Image Quality Index .....	37
5.3.2. Wald's Protocol .....	40
6. Experimental Results and Discussion .....	42
6.1 Visual Analysis .....	43
6.2 Quantitative Analysis .....	54
7. Conclusion .....	60
Bibliography .....	62
Appendix .....	73
Abstract in Korean .....	74

## List of Tables

[Table 1.1] Specification of Landsat-8 imagery .....	4
[Table 5.1] Definition and abbreviation of comparison analysis .....	35

# List of Figures

[Figure 1.1] Blackbody radiation curves and Lansat-8 TIRS SRF curves .....	3
[Figure 1.2] Scale-dependent urban analysis .....	6
[Figure 2.1] Thermal sharpening framework .....	13
[Figure 2.2] Pansharpening framework .....	16
[Figure 3.1] 2D scatter density plot between BT and NDVI .....	21
[Figure 3.2] 2D scatter density plot between BT and FVC .....	22
[Figure 3.3] 2D scatter density plot between BT and HSI .....	23
[Figure 3.4] 2D scatter density plot between BT and FUC .....	25
[Figure 4.1] Flowchart of proposed thermal sharpening algorithm .....	28
[Figure 5.1] Color composites of the study area for comparison .....	34
[Figure 5.2] Brightness Temperature map of the study area .....	34
[Figure 5.3] Overview of synthesis and consistency properties for evaluation of sharpened image quality .....	40
[Figure 6.1] The result of proposed MRHTS-FUC method .....	43
[Figure 6.2] Evaluation of results in subset A .....	45
[Figure 6.3] Evaluation of results in subset B .....	48
[Figure 6.4] Evaluation of results in subset C .....	51
[Figure 6.5] Result of image quality assessment for synthesis property .....	55
[Figure 6.6] Result of image quality assessment for consistency property .....	57

## List of Abbreviations

ASTER	Advanced Spaceborne Thermal Emission and Reflection radiometer
BT	Brightness Temperature
CC	Correlation Coefficient
CS	Component Substitution
DisTrad	Disaggregation of Radiometric Temperature
DN	Digital Number
DNB	Day/Night Band
ENVI	ENvironment for Visualizing Images
ERGAS	Erreur Relative Globale Adimensionnelle de Synthèse
FLAASH	Fast Line-of-sight Atmospheric Analysis of Spectral Hypercubes
FUC	Fractional Urban Cover
FVC	Fractional Vegetation Cover
HPM	High Pass Modulation
HSI	Human Settlement Index
LSR	Least Square Regression
IHS	Intensity-Hue-Saturation
HSI	Human Settlement Index
MRA	Multi Resolution Analysis

MRHTS-FUC	Modulation and Regression based Hybrid Thermal Sharpening using FUC
MRHTS-FVC	Modulation and Regression based Hybrid Thermal Sharpening using FVC
MRHTS-NDVI	Modulation and Regression based Hybrid Thermal Sharpening using NDVI
MRA	Multi Resolution Analysis
MS	MultiSpectral
NDVI	Normalized Difference Vegetation Index
NDWI	Normalized Difference Water Index
NTL	Night-Time Light
OLI	Operational Land Imager
PAN	PANchromatic
PCA	Principle Component Analysis
RTS-FUC	Regression based Thermal Sharpening using FUC
RTS-FVC	Regression based Thermal Sharpening using FVC
RTS-NDVI	Regression based Thermal Sharpening using NDVI
SFIM	Smoothing Filter-based Intensity Modulation
SRF	Spectral Response Function
SSIM	Structural SIMilarity

SWIR	Shortwave InfraRed
TIR	Thermal InfraRed
TIRS	Thermal InfraRed Sensor
TOA	Top-Of-Atmosphere
TsHARP	Temperature Sharpening
UIQI	Universal Image Quality Index
VI	Vegetation Index
VIIRS	Visible Infrared Imaging Radiometer Suite
VNIR	Visible and Near InfraRed

# 1. Introduction

## 1.1 Necessity for Thermal Sharpening

Thermal data is related to the emissivity of objects on the ground, and this property can account for biophysical phenomena (Kalma *et al.*, 2008; Roy *et al.*, 2014). Recently, thermal remote sensing using satellite sensors has made it possible to generate temperature maps over wide areas. However, a trade-off exists between spatial and spectral resolutions in any type of spaceborne remote sensing system (Chen *et al.*, 2014; Zhan *et al.*, 2011).

This limitation is especially evident in Thermal InfraRed (TIR) sensors. Radiometric features of TIR sensors can be explained by the laws of Planck, Stefan-Boltzmann and Wien. Planck's equation calculates the emitted electromagnetic radiance of a blackbody as a function of the absolute temperature of the given blackbody in Equation (1):

$$M_{\lambda, T} = \frac{2hc^2}{\lambda^5 (e^{hc/\lambda k T} - 1)} \quad (1)$$

where  $h$  is Planck's constant,  $c$  is the speed of light,  $\lambda$  is wavelength,  $k$  is Boltzmann's constant, and  $T$  is the temperature of a blackbody in Kelvin. The wavelength of maximum emittance

( $\lambda_{\max}$ ) and the total radiance for a blackbody ( $M_{tot}$ ) depend on the temperature of a blackbody, and can be described by Wien's displacement law and Stefan-Boltzmann's law as follows in Equations (2) and (3):

$$\lambda_{\max} = \frac{T}{A} \quad (2)$$

$$M_{tot} = \sigma T^4 \quad (3)$$

where  $A$  is Wien's constant equal to  $2897.8 \mu m K$  and  $\sigma$  is Stefan-Boltzmann constant equal to  $5.6697 \times 10^{-4} W/m^2 K^4$ . Based on both theorems, as the temperature of a blackbody increase, the wavelength of peak radiance shifts to shorter wavelengths and the total emitted radiance from the blackbody increases as shown in Figure 1.1.

Landsat 8's Thermal Infrared Sensor (TIRS) obtain radiation emitted by the earth on a range of 10-13  $\mu m$ . Following the sensor's Spectral Response Function (SRF), this range is effective to detect emittance of 300 K of a blackbody. The TIR band retrieves less total radiation than Visible-Near InfraRed (VNIR) and ShortWave InfraRed (SWIR) bands because of the region above 3  $\mu m$  of the electromagnetic spectrum. This region is characterized by emitted electromagnetic energy from natural materials which can be related to temperature related to the laws of Wien and Stefan-Boltzmann.

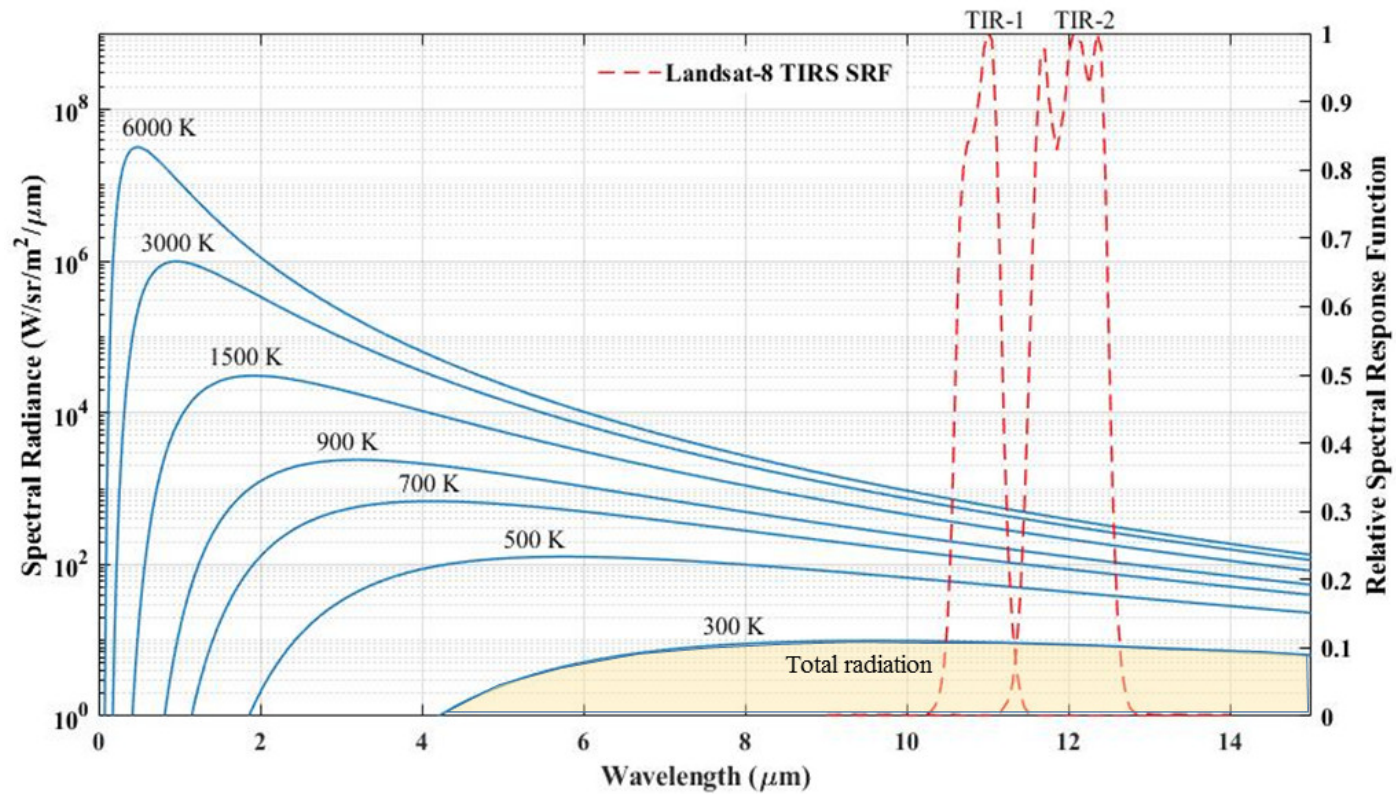


[Figure 1.1] Blackbody radiation curves and Lansat-8 TIRS SRF curves

Due to this radiometric characteristic, the spatial resolution of the TIR band is coarser than that of other Landsat-8 bands (Table 1.1). In addition, the limited spatial resolution of TIR sensors emphasizes the necessity for thermal sharpening of TIR imagery, also called thermal disaggregation or downscaling (Zhan *et al.*, 2013).

[Table 1.1] Specification of Landsat-8 imagery

Band	Spectral Region	Wavelength ( $\mu m$ )	Resolution (m)
B8	Pan	0.503–0.676	15
B1	Coastal/Aerosol	0.435–0.451	30
B2	Blue	0.452–0.521	30
B3	Green	0.533–0.590	30
B4	Red	0.636–0.673	30
B5	NIR	0.851–0.879	30
B6	SWIR-1	1.566–1.651	30
B7	SWIR-2	2.107–2.294	30
B9	Cirrus	1.363–1.384	30
B10	TIR-1	10.60–11.19	100
B11	TIR-2	11.50–12.51	100

## 1.2 Scale Dependency of Urban Remote Sensing

According to World Reference Data 2018 (Kaneda *et al.*, 2018), more than half of the world's population lives in urban areas. Correspondingly, rapid urbanization has brought socio-economic and ecological problems caused by disorderly urban sprawl (Li *et al.*, 2018). Urban remote sensing is an effective method for the long-term monitoring of urban growth and surface conditions. From a societal and environmental perspective, remote sensing of urban environmental conditions, such as urban surface temperature and urban vegetation, has become crucial. However, thermal remote sensing has been limited for applications in urban regions in comparison to other areas because accurate identification of urban structure types usually require images at a higher spatial resolution (Rashed and Jürgens, 2010).

The concept of urban structure type was suggested by Wickop *et al.* (1998) and used as a practical and appropriate method for urban surfaces analysis. Because of the scale dependency issue in urban areas to be described later, the process of urbanization must be monitored and simulated on a different scale. A relevant scale must be selected to analyze local and regional environmental effects (Banzhaf and Hofer, 2008). Figure 1.2 exemplifies the various impacts on urban areas that can be evaluated on different scales. Furthermore, urban dynamics and micro-climate analysis such as urban sprawl and urban heat island effect can be evaluated on the scale of urban land use and land cover. For studies on urban morphology, biotope structure

and settlement structure can be evaluated using urban remote sensing.

In the case of Landsat-8 TIRS, thermal imagery does not need to be sharpened for the use of urban land use and land cover for administrative and general urban analysis with a spatial resolution of 100-m. On the other hand, previous studies demonstrated the use of Landsat-8 OLI imagery with 30-m resolution for urban morphology analysis (Huang *et al.*, 2018). In terms of scale dependency, thermal sharpening can broaden the range of urban analysis from general to finer, site-specific analysis.

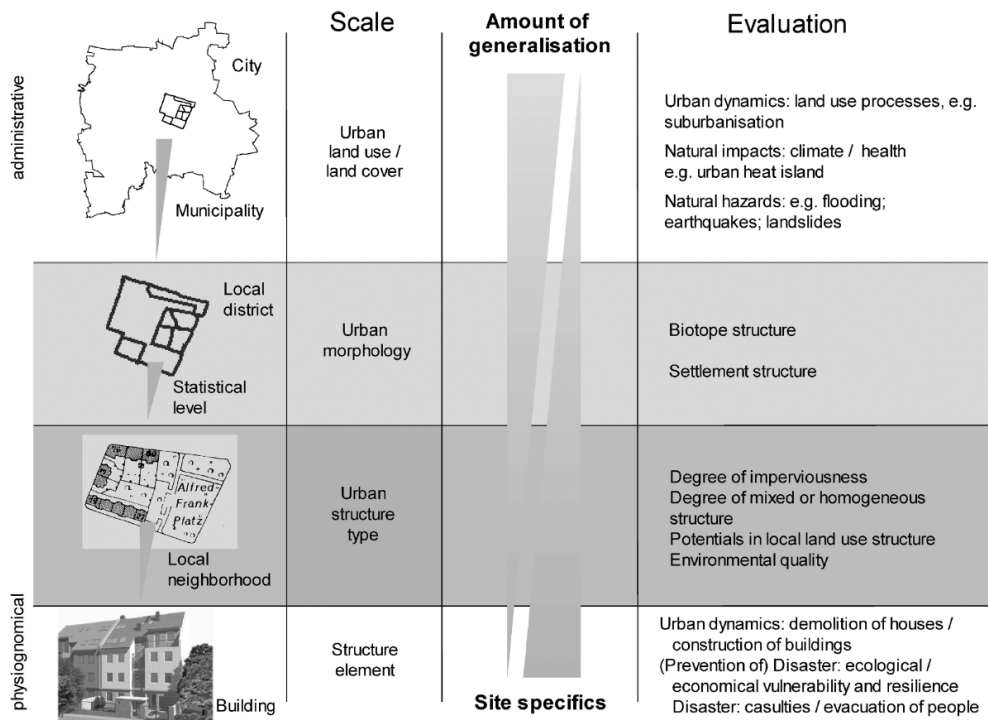


[Figure 1.2] Scale-dependent urban analysis

(Banzhaf and Hofer, 2008; modified after Wickop *et al.*, 1998)

## 1.3 Related Works

In the last few decades, various methods have been proposed for improving the spatial resolution of thermal imagery. One category of refined thermal sharpening algorithms uses statistical regression model. For example, statistically linear models include least square regression (Agam *et al.*, 2007; Jeganathan *et al.*, 2011; Kustas *et al.*, 2003) and multivariate regression (Jing and Cheng, 2010; Dominguez *et al.*, 2011).

Recently, complex non-linear statistical algorithms with additional multiple predictor variables have been proposed to improve the performance of the sharpening algorithm. These algorithms include least median square regression (Mukherjee *et al.*, 2014), artificial neural network (Bindhu *et al.*, 2013; Kolios *et al.*, 2013; Yang *et al.*, 2011), thin plate spline interpolation (Chen *et al.*, 2014), co-kriging method (Rodriguez-Galiano *et al.*, 2012), wavelet transformation (Moosavi *et al.*, 2015), and random forest regression (Hutengs and Vohland, 2016; Yang *et al.*, 2017).

Despite the high-accuracy of the non-linear regression model and statistically linear model, thermal sharpening procedures for radiometric surface temperature (DisTrad) (Agam *et al.*, 2007) and temperature sharpening (TsHARP) (Kustas *et al.*, 2003) algorithms have become the leading thermal sharpening methods. These methods are simple and effective in contrast to the complexity of the previously mentioned non-linear model.

Another category of thermal sharpening algorithms is called the modulation-based approach (Zhan *et al.*, 2011). The modulation models focus on the distribution of the radiance of a thermal image which is corrected by a visible band image. The motivation behind this principle is based on the Smoothing Filter-based Intensity Modulation (SFIM) known as Multi Resolution Approach (MRA) pansharpening. A pixel block intensity modulation algorithm (Guo and Moore, 1998) and an emissivity modulation algorithm (Stathopoulou and Cartalis, 2009) are examples of the modulation-based thermal sharpening algorithms.

With regard to the selection of input data for the sharpening algorithms, most methods including statistical regression models and modulation-based models have focused on the relationship between low-resolution TIR and high-resolution Vegetation Index (VI). In particular, these methods utilize the Normalized Difference Vegetation Index (NDVI) and Fractional Vegetation Cover (FVC) because densely vegetated areas tend to have relatively lower surface temperature (Agam *et al.*, 2007; Bindhu *et al.*, 2013; Dominguez *et al.*, 2011; Kustas *et al.*, 2003). For homogeneous land covers, such forest and agriculture, the VI-based thermal sharpening approach generates the high quality of performance.

Nevertheless, if the target scene includes heterogeneous land cover such as the variations in urban area as described in Section 1.2, thermal variation cannot be explained solely by NDVI (Yang *et al.*, 2011). Previous works indicated that the

VI-based disaggregation method of TIR was limited in heterogeneous areas (Bonafoni, 2016). For these reasons, several previous thermal sharpening algorithms for urban areas have focused on choosing other predictors instead of various VI, such as albedo (Merlin *et al.*, 2010), percent impervious surface area (Li *et al.*, 2011), temperature vegetation dryness index (Yang *et al.*, 2010), and normalized difference built-up index (Essa *et al.*, 2012). Considering that urban surface temperature is also related to land cover characteristics and urban form, an alternative index is required for the thermal sharpening process.

In terms of application of thermal data, most of the previous works integrated disaggregation methods to applications on a global scale such as evapotranspiration (Bindhu *et al.*, 2013; Bisquert *et al.*, 2016; Jiang and Weng, 2017; Olivera-Guerra *et al.*, 2017; Singh *et al.*, 2014), surface energy balance (Li *et al.*, 2017), and soil moisture estimation (Zhang *et al.*, 2014). Practical applications of thermal data, for example, are land cover classification (Sun and Schulz, 2015), urban heat islands (Dominguez *et al.*, 2011; Zakšek and Oštir, 2012), wildfires (Allison *et al.*, 2016; Cho *et al.*, 2018), and volcanic activity (Blackett, 2014; Zakšek *et al.*, 2015). As mentioned in the previous sections, these applications are still limited to the use of medium-resolution sensors such as Landsat-8 or Advanced Spaceborne Thermal Emission and reflection Radiometer (ASTER) products. Thermal sharpening is required for relatively medium-high spatial resolution imagery in order to expand the scope of TIR products for practical applications.

## 1.4 Objective of the Study

In thermal sharpening, the most important consideration is to produce detailed spatial properties while preserving spectral properties in sharpened results. For thermal sharpening in urban areas with heterogeneous land cover characteristics, the two crucial issues that require improvement are the selection of the input and the sharpening model.

First, a new input index must be chosen such that a new thermal sharpening algorithm will be able to surpass the performance of VI-based approaches. To effectively reflect the inherent detailed spatial information, this research developed a new index which is more related to the thermal variation of urban areas as an input for the thermal sharpening algorithm. Human Settlement Index (HSI) which is related to urban extents was estimated, and HSI was modified to Fractional Urban Cover (FUC) in order to increase the linearity and correlation with temperature. The selection of FUC index is based on an assumption that human settlement pattern is positively correlated with temperature variation in the thermal image.

Second, the selection of an appropriate sharpening model is required, which can preserve the spectral property of the sharpened result. To deal with the two issues, this study proposed a hybrid thermal sharpening framework using combined regression analysis and an approach using the modulation technique. A statistical regression model was established through the relationship between FUC and BT, and intensity was

extracted as an input of the modulation technique. Then, the sharpening process was performed using a High Pass Modulation (HPM) technique.

The objective of this study was to propose an improved thermal sharpening algorithm of TIR imagery for application in urban areas. For detailed urban analysis, a 100-m spatial resolution Landsat-8 TIRS imagery was sharpened to 30-m spatial resolution using Landsat-8 Operational Land Imager (OLI) and Visible Infrared Imaging Radiometer Suite (VIIRS) Night-Time Light (NTL) data. The main sections of this paper are structured as follows: Section 2 introduces previous thermal sharpening and pansharpening techniques. The proposed thermal sharpening method is defined in Section 3, and Section 4 outlines the selection of index and sharpening model. Section 5 describes experimental design including image quality assessments. Finally, Section 6 provides a discussion with regards to possible future advancements while Section 7 summarizes this study with a conclusion.

## 2. Frameworks of Thermal Sharpening and Pansharpening

### 2.1 Thermal Sharpening Framework

The purpose of thermal sharpening is to disaggregate the coarser spatial resolution of TIR images by introducing spatial detail from a finer resolution MultiSpectral (MS) image, without distorting the inherent spectral information. The thermal sharpening process consists of two main parts: the selection of an input index and the sharpening model. Figure 2.1 displays a brief overview of the framework that can include processes from previous studies of thermal sharpening. First, it is important to select an index that is highly correlated with temperature using high-resolution MS bands since the MS bands including VNIR and SWIR have different wavelength ranges from thermal band. Second, an appropriate sharpening model should be chosen to minimize spectral distortion. Previous thermal sharpening models can be roughly classified into statistical regression and the modulation-based approach. In the case of DisTrad and TsHARP, which are the most widely used algorithms, thermal sharpening is performed with statistical linear model using the NDVI and FVC as an input, respectively. The following two sections describe these two algorithms in more detail.

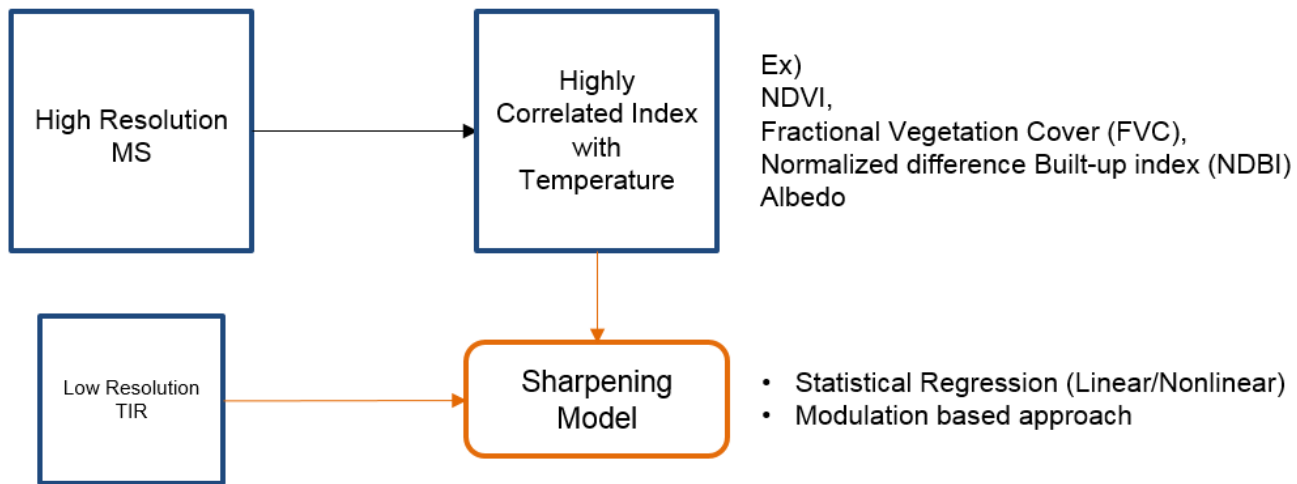


[Figure 2.1] Thermal sharpening framework

### 2.1.1 Disaggregation of Radiometric Temperature (DisTrad)

The DisTrad method focuses on the inverse relationship between temperature and NDVI using a 2nd order polynomial regression (Kustas *et al.*, 2003). The sharpening step of the algorithm is expressed by the following equations:

$$\widehat{T}_{LR} = f(NDVI_{LR}) = a_0 + a_1 NDVI_{LR} + a_2 NDVI_{LR}^2 \quad (4)$$

$$\Delta \widehat{T}_{LR} = T_{LR}^{obs} - \widehat{T}_{LR} \quad (5)$$

$$\widehat{T}_{HR} = f(NDVI_{HR}) + \Delta \widehat{T}_{LR} \quad (6)$$

where  $T_{LR}$  is the predicted temperature at low-resolution,  $T_{LR}^{obs}$  is the observed temperature from the satellite platform and  $T_{HR}$  is the predicted temperature at high-resolution. A linear least square regression was applied between low-resolution temperature imagery ( $T_{LR}$ ) and NDVI data ( $NDVI_{LR}$ ) in conjunction with the residual term ( $\Delta \widehat{T}_{LR}$ ) obtained by Equations (4) and (5). The low-resolution regression is then applied to the high-resolution NDVI data to estimate the disaggregated temperature imagery. Finally, to reduce the thermal sharpening error, the residual term derived from the regression at the low-resolution case is applied to the estimated temperature image at high-resolution in Equation (6).

### 2.1.2 Temperature Sharpening (TsHARP)

The TsHARP algorithm suggested by Agam *et al.* (2007), has a similar disaggregation processing step to the DisTrad, with the difference occurring only in the sharpening basis function. In TsHARP, the Fractional Vegetation Cover (FVC) was selected as the input for the sharpening basis function because this index is more physically correlated with temperature than NDVI. Hence, the sharpening basis function is replaced by Equation (7),

$$\begin{aligned}\widehat{T}_{LR} &= f(FVC_{LR}) \\ &= a_0 + a_1 \left(1 - \left(\frac{NDVI_{\max} - NDVI_{LR}}{NDVI_{\max} - NDVI_{\min}}\right)^{0.625}\right) = a_0 + a_1 FVC_{LR}\end{aligned}\quad (7)$$

$$\Delta \widehat{T}_{LR} = T_{LR}^{obs} - \widehat{T}_{LR}\quad (8)$$

$$\widehat{T}_{HR} = f(FVC_{HR}) + \Delta \widehat{T}_{LR}\quad (9)$$

where  $NDVI_{\max}$  and  $NDVI_{\min}$  are the maximum and minimum value of NDVI in the single scene of data. The remainder of the thermal sharpening process is equal to that of DisTrad.

## 2.2 Pansharpener Framework

### 2.2.1 General Pansharpener Approach

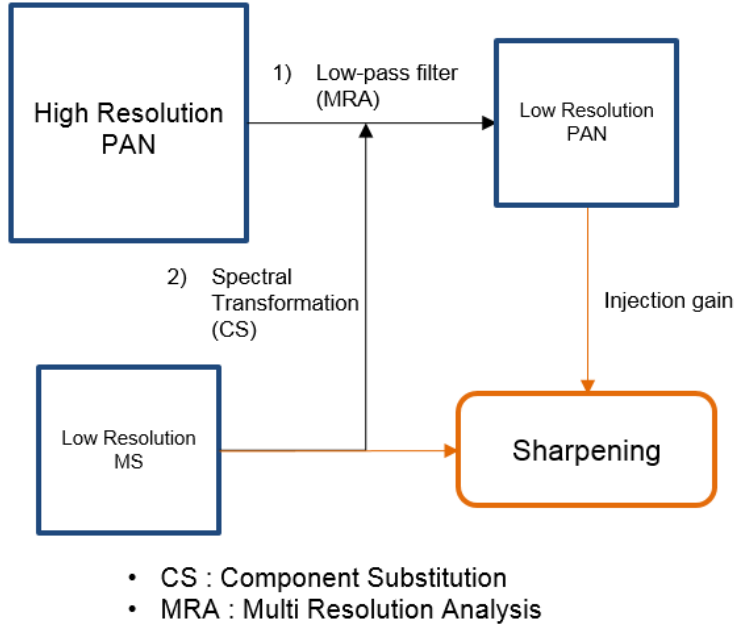


[Figure 2.2] Pansharpener framework

Previous pansharpener methods can be divided into two categories: Component Substitution (CS) and MRA approaches. These two categories differ by the method of estimating low-resolution PAN (Figure 2.2). Vivone *et al.* (2015) suggested a general formulation of the pansharpener for both CS and MRA methods using the following equation:

$$D_{HR,b}(x,y) = D_{LR,b}(x,y) + g_b(x,y) \circ (D_{HR,p}(x,y) - D_{LR,p}(x,y)) \quad (10)$$

where  $b = 1, \dots, N$  indicates the  $N$  bands of low-resolution MS image and pixel value at row  $x$  and column  $y$  is denoted by  $D(x, y)$ . The  $b$  th band of the interpolated, but low-resolution scale MS image is represented as  $D_{LR, b}$ , and  $D_{HR, p}$  indicates that the PAN image with high-resolution scale. Finally,  $\circ$  denotes a pixel-wise operator, and  $g_b(x, y)$  expresses the injection gain.

In the CS-based pansharpening method, spatial details are injected into the interpolated higher resolution of MS bands ( $D_{LR, b}$ ) using the PAN image ( $D_{HR, p}$ ) and the spectral transformed image ( $D_{LR, p}$ ) retrieved through transformation techniques such as IHS (Intensity-Hue-Saturation) and PCA (Principle Component Analysis). However, considering the thermal sensor only consists of a single band image, application of the CS-based approach with spectral transformation to the thermal sharpening algorithm is difficult. On the other hand, in the MRA-based pansharpening method, the spatial details are extracted from the PAN image acquired linear shift invariant low-pass filtering ( $D_{LR, p}$ ). Again, given there is only a single thermal band available, the MRA-based pansharpening method can only be applied for single-band thermal sharpening processing.

## 2.2.2 High Pass Modulation (HPM) Method

MRA-based pansharpening methods can be sorted by the usage of low-pass filtering. Liu (2000) applied a box-type moving average filter to pansharpening an algorithm called SFIM or the high pass modulation (HPM) method. According to Alparone *et al.* (2017) and Vivone *et al.* (2014), the HPM method can obtain outstanding results which preserved spectral features and improved spatial details. The HPM algorithm can be expressed by the following injection gain ( $g_b$ ):

$$g_b(x, y) = \frac{D_{LR,b}(x, y)}{D_{LR,p}(x, y)} \quad (11)$$

The injection gain from equation (11) can be applied to the general formulation of the pansharpening method in equation (10) for injecting spatial details. Finally, the HPM method is organized by equation (12):

$$\begin{aligned} D_{HR,b}(x, y) &= D_{LR,b}(x, y) + \frac{D_{LR,b}(x, y)}{D_{LR,p}(x, y)} \circ (D_{HR,p}(x, y) - D_{LR,p}(x, y)) \\ &= D_{LR,b}(x, y) \circ \frac{D_{HR,p}(x, y)}{D_{LR,p}(x, y)} \end{aligned} \quad (12)$$

## 3. Input Variable Selection for Thermal Sharpening in Urban Areas

### 3.1 Human Settlement Index (HSI) from VIIRS NTL

The VIIRS DNB collects global low-light imaging of the Earth at night. The NTL from DNB data can detect electric lighting present on the Earth's surface. These products explain the locations where artificial lighting is present and provides a measure of the brightness as observed from space. NTL imagery can therefore reflect the presence of human activity. In more detail, the intensity of nighttime light from cities is closely related to population density and settlement pattern, and the NTL data are used to map urban areas and human settlements (Elvidge *et al.*, 2007).

However, due to the low spatial resolution of VIIRS DNB NTL data (750-m), there is an inevitable information loss of spatial patterns in NTL data. It is not appropriate to analyze areas with small proportional settlement patterns such as towns and villages, as such analyses will result in an overestimation of urban extents (Lu *et al.*, 2008). As a response to these limitations, the HSI was suggested by Lu *et al.* (2008) which accounts for the spatial resolution of NTL data when extracting finer-scale residential sites from NTL and NDVI data.

Because NDVI data are normalized from -1 to 1, the normalization of Digital Number (DN) values of NTL data was required to match this difference. Normalization of NTL data is expressed by the following equation (13):

$$NTL_{nor} = \frac{NTL - NTL_{\min}}{NTL_{\max} - NTL_{\min}} \quad (13)$$

where  $NTL_{nor}$  is the normalized value of VIIRS NTL image,  $NTL_{\max}$  and  $NTL_{\min}$  are the minimum and maximum value of NTL data. Combining these two normalized indices, the HSI is represented as:

$$HSI = \frac{(1 - NDVI) + NTL_{\min}}{(1 - NTL_{nor}) + NDVI + NTL_{nor} \cdot NDVI} \quad (14)$$

From the HSI, select land cover which include a waterbody have resulted in a overestimation of HSI value than that of other land cover types (Li *et al.*, 2018). Hence, a mask was defined using a higher value of Normalized Difference Water Index (NDWI) which was then the mask was applied to the HSI image to reduce the impact of the waterbody.

## 3.2 Statistical Analysis between BT and Input Indices

2D scatter density plots and correlations were analyzed in order to evaluate HSI as an input of thermal sharpening by comparing the VI-based indices. The correlation coefficient ( $r_{kl}$ ) was calculated by the following equation:

$$r_{kl} = \frac{S_{kl}}{S_k S_l} \quad (15)$$

where  $S_{kl}$  is covariance,  $S_k$  and  $S_l$  are the standard deviation of  $k$  and  $l$  image, respectively. First, for the input data using an NDVI, Figure 3.1 depicts the 2D scatter density plot between BT and NDVI.

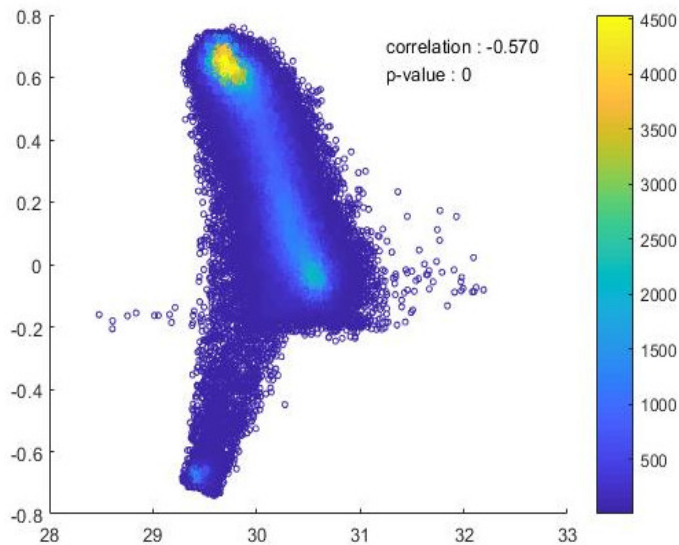


[Figure 3.1] 2D scatter density plot between BT (x-axis) and NDVI (y-axis)

In Figure 3.2, the NDVI demonstrates the physical assumption of the NDVI-based thermal sharpening algorithm. However, the correlation is weakened by the lower NDVI value of -0.3 due to the dominant influence of waterbody areas.

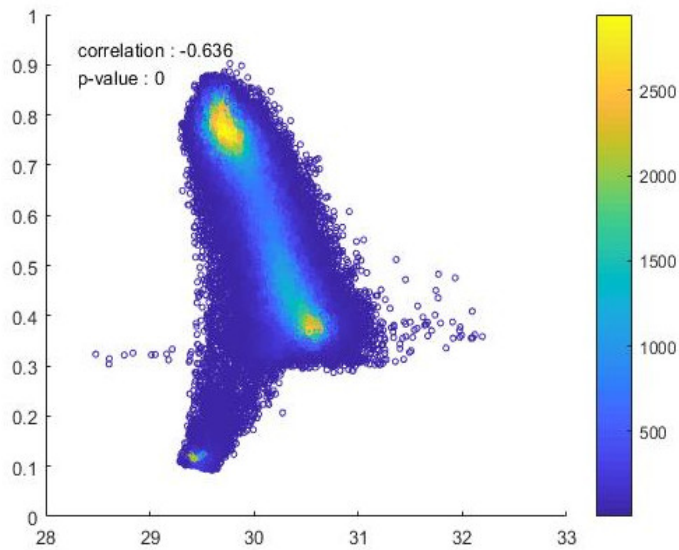


[Figure 3.2] 2D scatter density plot between BT (x-axis) and FVC (y-axis)

In the case of FVC, the 2D scatter density plot is more correlated with a negative correlation (Figure 3.2). Similar to the NDVI-based index, this result is affected by error due to the presence of water bodies, which consequently corresponds with potential error in spatial detail in the thermal sharpening algorithm. On the other hand, Figure 3.3 displays a positive relationship between BT and HSI, and the correlation coefficient of 0.847 is the highest value among all of the other indices.

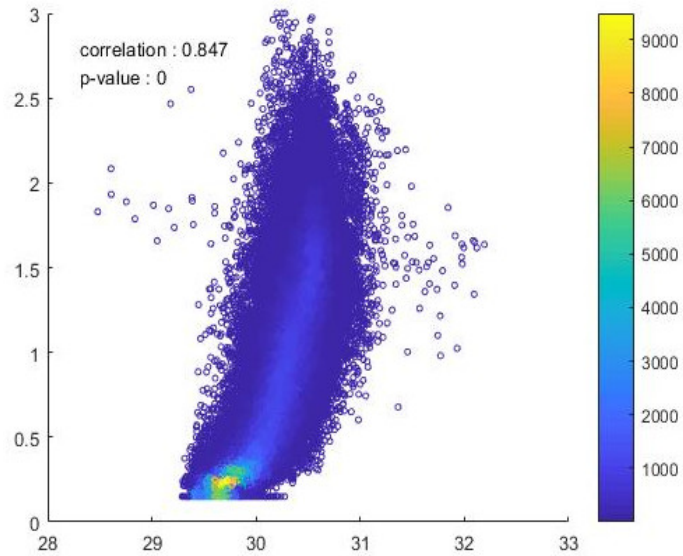


[Figure 3.3] 2D scatter density plot between BT (x-axis) and HSI (y-axis)

However, the 2D scatter density plot between BT and HSI returns a concentrated pattern in the range of HSI values between 0 and 0.5. In terms of linearity, it is difficult to determine whether this trend demonstrates a direct relationship between HSI and BT.

### 3.3 Suggestion of a New Index

#### : Fractional Urban Cover (FUC)

In this study, a new index was proposed to increase the linearity and correlation between input index and BT. This index has been modified from the mathematical definition of the FVC—an NDVI-based index. The equation of FVC is as follows:

$$FVC = 1 - \left( \frac{NDVI_{\max} - NDVI}{NDVI_{\max} - NDVI_{\min}} \right)^{0.625} \quad (16)$$

In the case of Equation (16), NDVI is normalized and expressed as an exponential function to increase the linearity of the scatter density plot with BT. This study focused on this tendency and introduced a new index, Fractional Urban Cover (FUC). The proposed FUC index is expressed by the following equation:

$$FUC = \left( \frac{HSI_{\max} - HSI}{HSI_{\max} - HSI_{\min}} \right)^n \quad (17)$$

where  $HSI_{\max}$  and  $HSI_{\min}$  are the maximum and minimum value of  $HSI$  in the single scene of data. The coefficient  $n$  is numerically determined at the maximum value of the correlation coefficient between FUC and BT (Appendix A.1). Figure 3.4 demonstrates the highest correlation coefficient value and linearity between FUC and BT in the 2D scatter density plot.

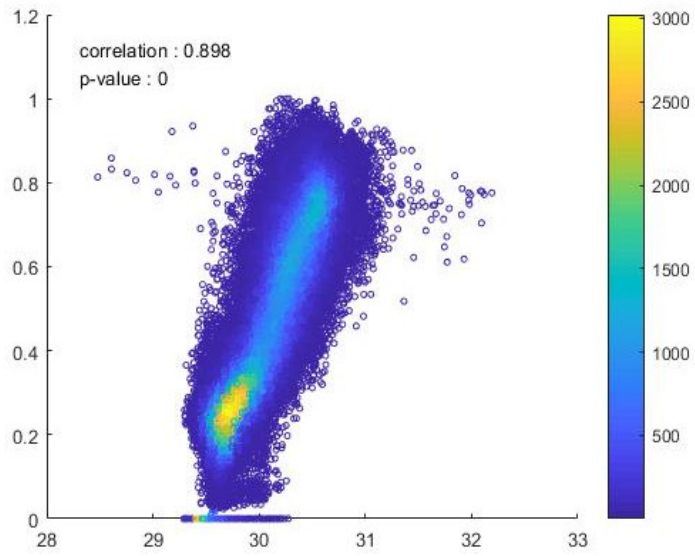


[Figure 3.4] 2D scatter density plot between BT (x-axis) and FUC (y-axis)

## 4. Modulation and Regression based Hybrid Thermal Sharpening Using FUC Index

### 4.1 Workflow

A flowchart of the proposed disaggregation method is described in Figure 4.1. Originally, the distributed Level 1 TIR data was already resampled to 30-m resolution by cubic convolution resampling (Roy *et al.*, 2014). To obtain the original resolution of the TIR image at 100-m resolution, an aggregation procedure was conducted on the Level 1 TIR data. However, the ratio between high- and low-resolution was rounded to 3 for efficient image processing. In other words, the original resolution of the TIR dataset was assumed to be 90-m instead of 100-m because NASA (National Aeronautics and Space Administration) conducted precise co-registration for Landsat products (Roy *et al.*, 2014). Also, TIR-2 band data were excluded because of its larger calibration uncertainty as reported in Landsat-8 Calibration Notices from USGS (<https://www.usgs.gov/land-resources/nli/landsat/landsat-8-oli-and-tirs-calibration-notices>).

The main inputs of this method are only the TIR-1 band as Brightness Temperature (BT), NDVI from Landsat-8 Top-Of-Atmosphere (TOA) reflectance and NTL data from the VIIRS DNB image. The NTL image was normalized and resampled to the 30-m resolution to match the Landsat OLI

resolution. Then, HSI was calculated using NDVI and NTL. For the robustness of the thermal sharpening input from the perspective of correlation and linearity, this study defined the FUC, based on HSI. The relationship between BT and FUC was established as a statistically linear model, and the output of the model was used as an intensity image for the HPM algorithm. After HPM sharpening, the residual term at low-resolution scale was corrected. Finally, image quality metrics were used to evaluate the sharpened image accuracy in terms of spectral preservation and spatial details.

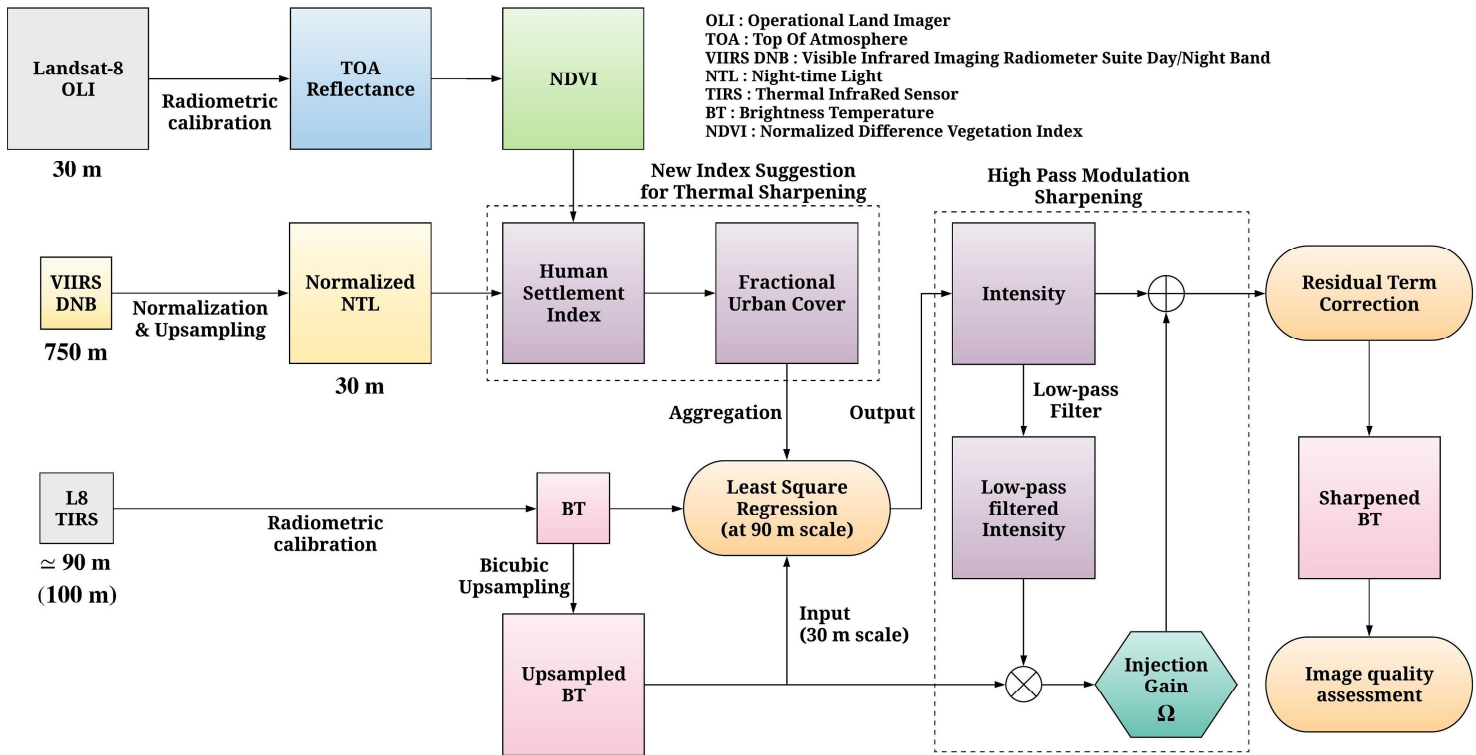


[Figure 4.1] Flowchart of proposed thermal sharpening algorithm

## 4.2 Preprocessing

To obtain at-sensor spectral radiance, TOA reflectance, or at-sensor BT, the DN values must be converted using a radiometric calibration process (Chander *et al.*, 2009). First, the DN format of the image data was converted to an at-sensor spectral radiance ( $L_\lambda$ ) as follows:

$$L_\lambda = G_{rescale} \cdot DN + offset \quad (18)$$

where  $G_{rescale} = \frac{L_{max} - L_{min}}{DN_{max} - DN_{min}}$  is a rescaling gain factor,  $Offset = L_{min} - G_{rescale} DN_{min}$  is a rescaling offset factor,  $L_{max}$  and  $L_{min}$  are spectral at-sensor radiances that are scaled to  $DN_{max}$  and  $DN_{min}$ , respectively, and the unit of  $L_\lambda$  is  $W/(m^2 sr \mu m)$ . Based on the calculated at-sensor spectral radiance, TOA reflectance  $\rho_\lambda$  and at-sensor BT ( $BT$ ) can be obtained by employing Equations (19) and (20):

$$\rho_\lambda = \frac{\pi \cdot L_\lambda \cdot d^2}{ESUN_\lambda \cdot \cos \theta_s} \quad (19)$$

$$BT = \frac{K_2}{\ln\left(\frac{K_1}{L_\lambda} + 1\right)} \quad (20)$$

where  $d$  is an earth-sun distance in astronomical unit,  $ESUN_\lambda$  is solar irradiance,  $\theta_s$  is solar zenith angle, and  $K_1$ ,  $K_2$  are calibration constants.

In this study, the DN of OLI imagery were converted to TOA reflectance by using the Fast Line-of-sight Atmospheric Analysis of Spectral Hypercubes (FLAASH) model (Felde *et al.*, 2003) using ENvironment for Visualizing Images (ENVI) software. This allows for the DN values of VNIR and SWIR images to be converted to TOA reflectance and that of TIR to be converted to BT. The converted TOA reflectance and BT were then used as input data for both the proposed and comparative thermal sharpening algorithms. The use of TOA reflectance reduced the effect of reflective solar radiance following the Earth-sun-satellite geometry (Murphy *et al.*, 2016).

### 4.3 First Step : Intensity Generation Using Statistical Regression between FUC and BT

After radiometric calibration, statistical regression was used to obtain the intensity component from the FUC index. Due to the spatial features of FUC in urban areas, the intensity was used to obtain high spatial resolution and a high-frequency temperature component for urban areas instead of the NDVI-based index. Least square regression was applied in this study and its expression is given as follows:

$$BT_{LR} = f(FUC_{LR}) = a_0 + a_1 \cdot FUC_{LR} \quad (21)$$

where  $BT_{LR}$  is brightness temperature at low-resolution and  $FUC_{LR}$  is fractional urban cover at low-resolution. The low-resolution regression, then, is applied to the high-resolution FUC data to estimate the intensity component.

$$I_{HR} = f(FUC_{HR}) \quad (22)$$

where  $I_{HR}$  is the intensity component, and  $FUC_{HR}$  is fractional urban cover at high-resolution.

## 4.4 Second Step : Application of HPM Sharpening

The extracted intensity in section 4.3 was used as an input for the HPM sharpening method. The equation of HPM sharpening is summarized by the following equation:

$$D_{HR,b}(x,y) = D_{LR,b}(x,y) \circ \frac{D_{HR,p}(x,y)}{D_{LR,p}(x,y)} \quad (23)$$

In equation (23), the intensity image is regarded as PAN and was applied to thermal sharpening. In this study,  $3 \times 3$  moving average low-pass filter ( $h_{LP}$ ) was set to generate a low-resolution intensity image as follows:

$$h_{LP} = \frac{1}{9} \begin{bmatrix} 1 & 1 & 1 \\ 1 & 1 & 1 \\ 1 & 1 & 1 \end{bmatrix} \quad (24)$$

Thermal sharpening using the HPM method, including the low-pass filter, can be expressed by equation (24):

$$\widehat{BT}_{HR} = BT_{LR} \circ \frac{I_{HR}}{I_{HR} \otimes h_{LP}} \quad (25)$$

where  $\widehat{BT}_{HR}$  is predicted temperature at high-resolution and  $\otimes$  denotes a convolution operator in the sharpening process.

## 5. Experimental Design

### 5.1 Study Area and Materials

To verify the effectiveness of the proposed algorithm in urban areas, the study area was selected to be the Seoul metropolitan area, one of the mega-cities in East Asia. This area is considered to be suitable for sharpening method analysis in urban areas because of the presence of many heterogeneous urban land cover. For the processing and evaluation of the proposed algorithm in this study, freely accessible and periodically available Landsat-8 Level-1 OLI, TIRS, and VIIRS DNB NTL datasets were acquired from the USGS Earth Explorer website and NOAA National Centers for Environmental Information website, respectively.

In the case of Landsat imagery, the datasets were taken at 02:11:08 GMT (11:11:08 local time), August 26<sup>th</sup>, 2017 from 116 path and 34 row in the WRS-2. Landsat-8 OLI and TIRS imagery were then converted to TOA reflectance and brightness temperature through radiometric calibration (Figure 5.1 and 5.2). For the NTL image, VIIRS DNB Cloud-Free Composites, which are average radiance composite images, were used in this research because this composite data excluded the impact from stray light, lightning, lunar illumination, and cloud-cover. Based on the date of the Landsat-8 image, the image was generated by averaging over the month of August, and was chosen to be applied for the proposed sharpening algorithm.

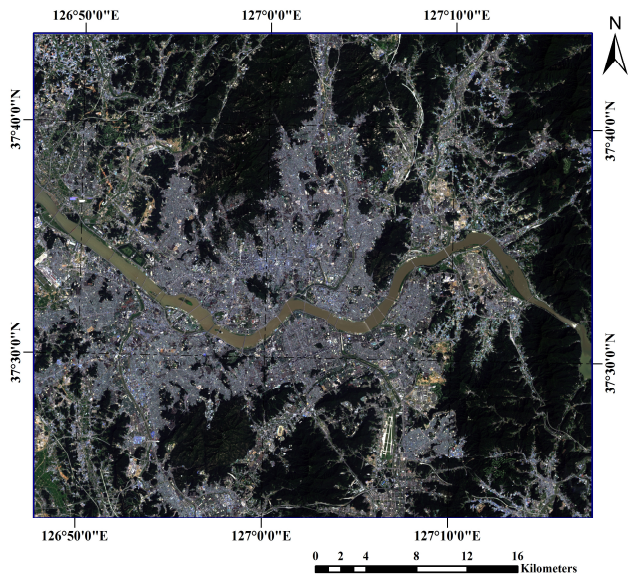


[Figure 5.1] Color composites of the study area for comparison

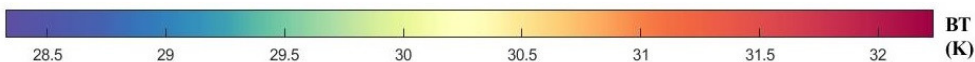
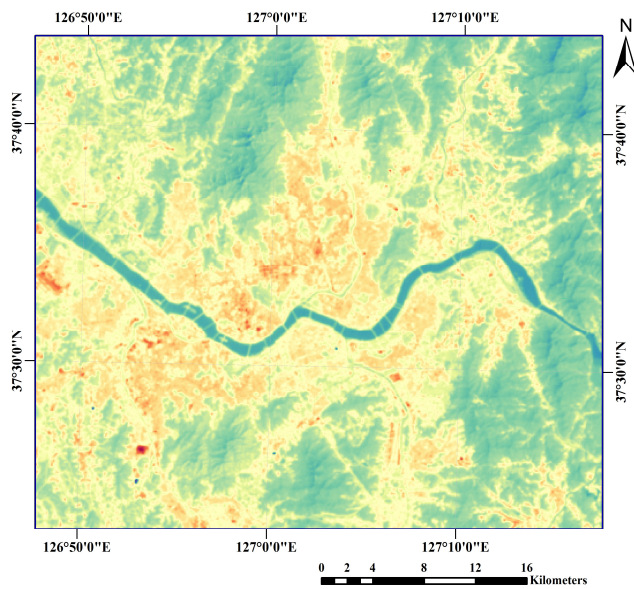


[Figure 5.2] Brightness Temperature map of the study area

## 5.2 Algorithm Selection for Comparison Analysis

[Table 5.1] Definition and abbreviation of comparison analysis

Algorithm Definition	Abbreviation
Regression based Thermal Sharpening using NDVI (Disaggregation of Radiometric Temperature)	RTS-NDVI (DisTrad)
Regression based Thermal Sharpening using FVC (Temperature Sharpening)	RTS-FVC (TsHARP)
Regression based Thermal Sharpening using FUC	RTS-FUC
Modulation and Regression based Hybrid Thermal Sharpening using NDVI	MRHTS-NDVI
Modulation and Regression based Hybrid Thermal Sharpening using FVC	MRHTS-FVC
Modulation and Regression based Hybrid Thermal Sharpening using FUC (Proposed)	MRHTS-FUC

To evaluate the performance of the proposed algorithm, five algorithms were selected for comparison and are indicated in Table 5.1. For the selection and evaluation of the comparison algorithms, this study focused on two criteria. The first requirement was to compare the proposed hybrid thermal sharpening framework with the thermal sharpening method used in the statistical regression method including DisTrad and TsHARP. In this manner, this study evaluated the performance

of the sharpening framework, the proposed Modulation and Regression based Hybrid Thermal Sharpening (MRHTS) and the Regression based Thermal Sharpening (RTS). In the case of modulation based thermal sharpening, the performance was lower than that of the RTS model (Chen *et al.*, 2014). Thus, modulation based thermal sharpening was excluded from the comparison algorithm. The second requirement was to evaluate the effect of input variables in thermal sharpening. Namely, the NDVI used in DisTrad, the FVC used in TsHARP, and the proposed FUC indices were selected as input variables for comparison.

## 5.3 Image Quality Assessment

### 5.3.1 Image Quality Index

To evaluate the quantitative image quality, four widely used quality indices were selected in this study. First, Erreur Relative Globale Adimensionnelle de Synthèse (ERGAS) is a useful index to evaluate the overall quality of the disaggregated image (Zhan *et al.*, 2011). This metric represents the degree to which the disaggregated image and the reference image differ. The ERGAS is defined in Equation (26) and (27) as follows:

$$RMSE = \sqrt{\frac{1}{M \cdot N} \sum_{m=1}^M \sum_{n=1}^N (F(m,n) - R(m,n))^2} \quad (26)$$

$$ERGAS = \frac{100}{\beta} \sqrt{\frac{1}{N} \sum_{i=1}^N \left( \frac{RMSE_i}{\mu_i} \right)^2} \quad (27)$$

where  $F(m,n)$  and  $R(m,n)$  represent the pixel values of the fused image,  $F$ , and the reference image  $R$ , at the  $m$  th column and  $n$  th row, and  $M \times N$  is the size of the reference image.  $\beta$  is the scale ratio between the pixel sizes of the SWIR image and the BT image,  $RMSE_i$  is the RMSE between the  $i$  th fused band and the reference band, and  $\mu_i$  is the mean of the  $i$  th reference band. Thus, a small value of ERGAS means a low level of spectral distortion is present in the disaggregated image.

The Correlation Coefficient (CC) is also used to assess the fused images. The CC of a fused image and its reference image reflects the similarity of spectral information. The formulation in Equation (28) is as follows:

$$CC = \frac{\sum_{m=1}^M \sum_{n=1}^N (F(m,n) - \mu_F)(R(m,n) - \mu_R)}{\sqrt{\sum_{m=1}^M \sum_{n=1}^N (F(m,n) - \mu_F)^2 \sum_{m=1}^M \sum_{n=1}^N (R(m,n) - \mu_R)^2}} \quad (28)$$

where  $\mu_F$  and  $\mu_R$  are the mean of the fused image and the reference image, respectively. If the two images are correlated, the CC is close to 1, which implies that the spectral features of the original image were preserved well during the disaggregation process.

To evaluate the degree of spatial distortion, the Structural SIMilarity index (SSIM) is also considered as an image quality index. The SSIM is based on the three terms, namely the luminance ( $l$ ), contrast ( $c$ ), and structural term ( $s$ ) (Wang *et al.*, 2004). The SSIM is defined in Equation (29) as follows:

$$SSIM = [l(m,n)]^\alpha \cdot [c(m,n)]^\beta \cdot [s(m,n)]^\gamma \quad (29)$$

where

$$l(m,n) = \frac{2\mu_x\mu_y + C_1}{\mu_x^2 + \mu_y^2 + C_1} \quad (29)$$

$$c(m,n) = \frac{2\sigma_x\sigma_y + C_2}{\sigma_x^2 + \sigma_y^2 + C_2} \quad (30)$$

$$s(m, n) = \frac{\sigma_{xy} + C_3}{\sigma_x \sigma_y + C_3} \quad (31)$$

where  $\alpha$ ,  $\beta$ , and  $\gamma$  are parameters used to adjust the relative importance of the three components, and the constant  $C_1$ ,  $C_2$  and  $C_3$  are included to avoid instability when the denominator is very close to zero.  $\sigma_{FR}$  is the covariance matrix between the fused image and the reference image, and  $\sigma_F$  and  $\sigma_R$  are the standard deviations of the fused image and the reference image, respectively. If its value is close to 1, the quality of the sharpened image is adequate. When suppose  $\alpha = \beta = \gamma = 1$  and  $C_3 = C_2/2$ , the SSIM simplifies to following equation (32):

$$SSIM = \frac{(2\mu_x \mu_y + C_1)(2\sigma_x \sigma_y + C_2)}{(\mu_x^2 + \mu_y^2 + C_1)(\sigma_x^2 + \sigma_y^2 + C_2)} \quad (30)$$

Also, the image quality Q index, also known as the Universal Image Quality Index (UIQI), reflects the degree of structural distortion, loss of correlation, and luminance distortion (Wang and Vovik, 2002). The UIQI, which can evaluate spectral and spatial properties simultaneously, is defined in Equation (29) as follows:

$$UIQI = \frac{\sigma_{FR}}{\sigma_F \sigma_R} \cdot \frac{2|\mu_F| |\mu_R|}{|\mu_F|^2 |\mu_R|^2} \cdot \frac{2\sigma_F \sigma_R}{\sigma_F^2 + \sigma_R^2} \quad (30)$$

The UIQI was applied to the sharpened results with an  $8 \times 8$  distinct window. If the value of UIQI approaches 1, the quality of the fused image is deemed sufficient.

### 5.3.2 Wald's Protocol

In this study, no reference image was available to objectively evaluate the quality of the sharpened thermal image generated using the MS image and low-resolution thermal image. The Wald's protocol was used to overcome this problem. The two methods are referred to as the synthesis and the consistency properties, which are commonly used to assess the quality of the fused image (Vivone *et al.*, 2015), are presented in Figure 5.3..

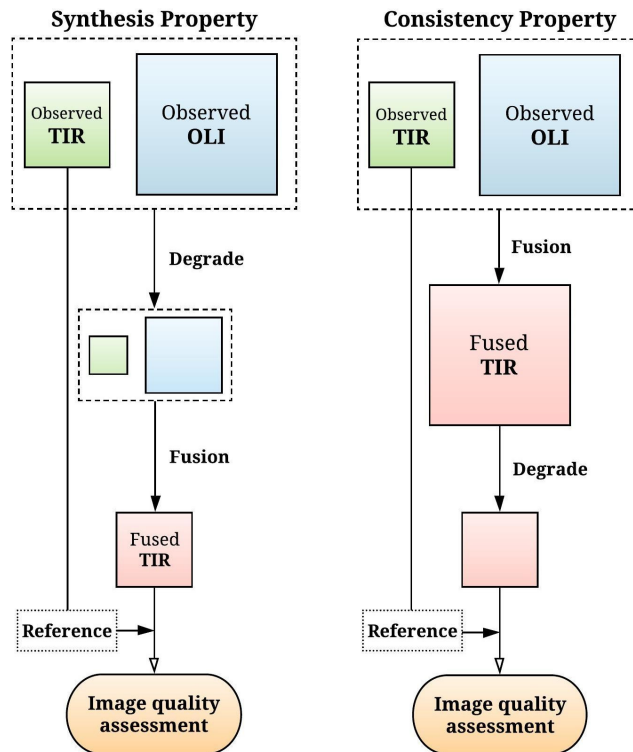


[Figure 5.3] Overview of synthesis and consistency properties for evaluation of sharpened image quality

Firstly, the synthesis property considers the disaggregated image to be as close to identical to the acquired input image as possible. However, at full-resolution scale, assessment of the synthesis property is not possible. Alternatively, assuming that the sharpening method is invariant to the spatial scale, the input images of thermal sharpening were degraded by the scale ratio between the pixel sizes of the OLI image and the BT image. The degraded images were used as an input for the disaggregation method, and the degraded fused image was compared to the original observed BT image as a reference.

Secondly, the consistency property reflects the degree to which the spatially degraded fused image is identical to the originally observed BT image. Cubic convolution interpolation was applied for image degradation of the synthesis and consistency properties. To validate the evaluation process, both synthesis and the consistency properties were applied to the experimental assessments.

## 6. Experimental Results and Discussion

Experiments were conducted to evaluate the performance of the modulation and regression based hybrid thermal sharpening with the FUC index as an input (MRHTS-FUC). The MRHTS-FUC algorithm was compared with the selected five algorithms described in Section 5.2 in terms of models and input variables. Khan *et al.* (2009) suggested that one or more protocols should be used to evaluate the tested sharpening technique because the technique may only be suitable for a specific protocol. In light of this proposition, the present study evaluated the disaggregation methods focused on the synthesis and consistency properties using the image quality indices mentioned in Section 5.3. However, since the two protocols are alternative evaluation methods that validate at a lower spatial scale, due to the absence of a reference image, visual analysis as well as quantitative analysis based on the two protocols must be performed for fair evaluation of the algorithm (Wang and Vovik, 2002).

## 6.1 Visual Analysis

The proposed thermal sharpening method, MRHTS-FUC, was compared with the RTS-NDVI (DisTrad), RTS-FVC (TsHARP), RTS-FUC, MRHTS-NDVI and MRHTS-FVC methods. Figure 6.1 displays the result of the proposed method (MRHTS-FUC). To qualitatively evaluate the results, three subsets of the sharpened images, A, B, and C in Figure 6.1 were obtained and directly compared with other methods using the selected subset areas as shown in Figures 6.2-4. As a result, notable features of the results from the proposed method were observed in qualitative analysis.

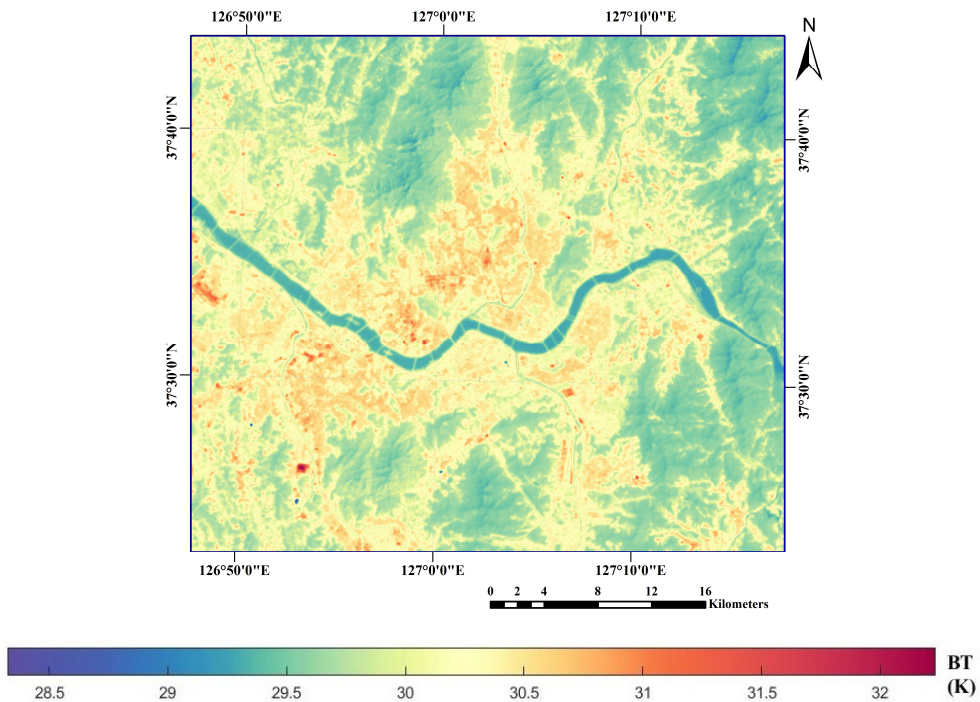


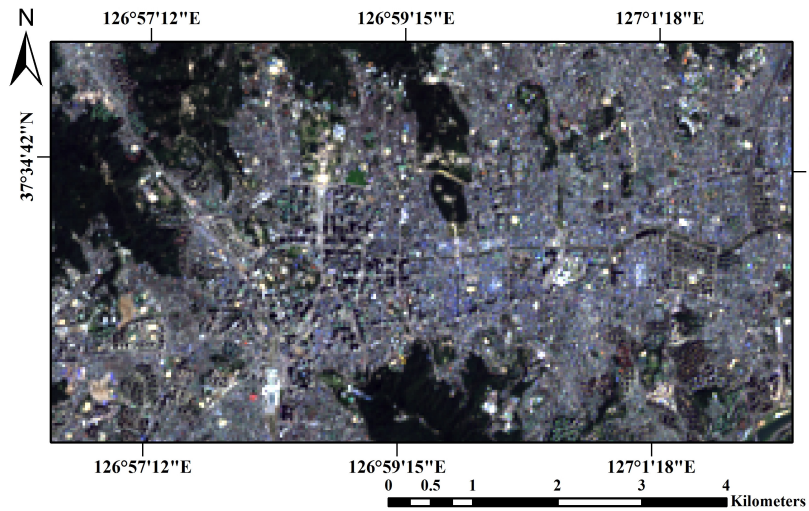
[Figure 6.1] The result of proposed MRHTS-FUC method

First, in terms of input variable selection, the proposed algorithm using FUC index performed well on urban areas, including spatially-preserving high-frequency temperature components (Figures 6.2-4 (h)). The result of BT in NDVI-based sharpening algorithms (RTS-NDVI and MRHTS-NDVI) presented an increase in sharpness for the vegetation area (Figure 6.3 (c)), but no sharpness increase in the urban area (Figures 6.2-4 (c) and (f)). In the case of the FVC-based algorithms (RTS-FVC and MRHTS-FVC) revealed better sharpness in urban areas than NDVI-based algorithms, but the increase of sharpness in urban areas was weaker in contrast to the algorithms using FUC index (RTS-FUC and MRHTS-FUC; Figures 6.2-4 (d), (e), (g) and (h)). The FUC index-based models showed comprehensive spatial details in both urban and vegetation areas (Figures 6.2-4 (e) and (h)).

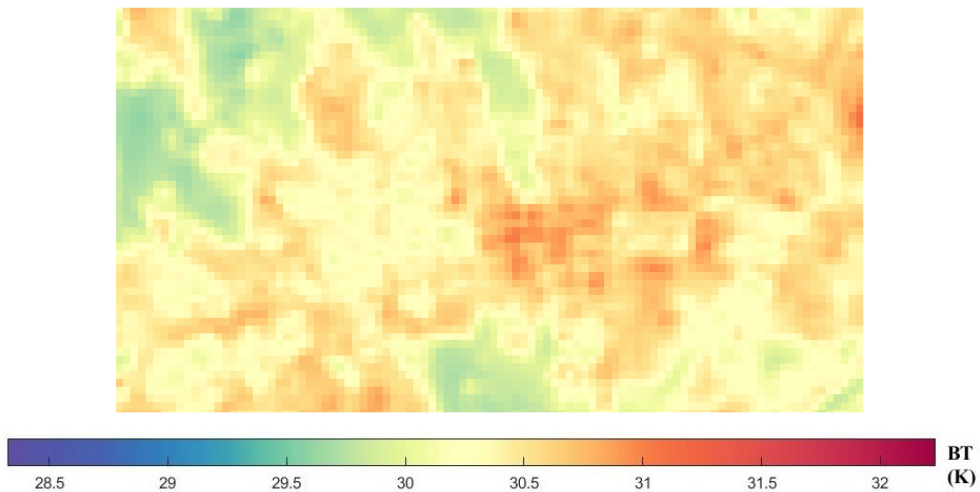
Second, with regards to the sharpening model, the proposed MRHTS framework presented a reduction in the overall sharpness of the image for all input indices. In the case of NDVI and FVC, the sharpness of the vegetation area was decreasing in the MRHTS model (Figures 6.3 (c), (d), (f) and (g)). Also, the decrease of overall sharpness was observed in the proposed FUC index (Figures 6.2-6.4 (e) and (h)). As shown through the visual analysis of the results, this experiment confirmed that the proposed FUC index can provide visually satisfactory results with regards to the original BT image.

Meanwhile, in the vicinity of the waterbody, the RTS-NDVI algorithm illustrated clearer sharpening result in comparison to

the other methods (Figure. 6.4 (c)). The FUC-based algorithms (RTS-FUC and MRHTS-FUC) displayed a tendency to under-sharpen in regions consisting of a waterbody, and FVC-based algorithms showed ringing artifacts nearby water boundaries (Figures 6.4 (d), (e), (g) and (h)).

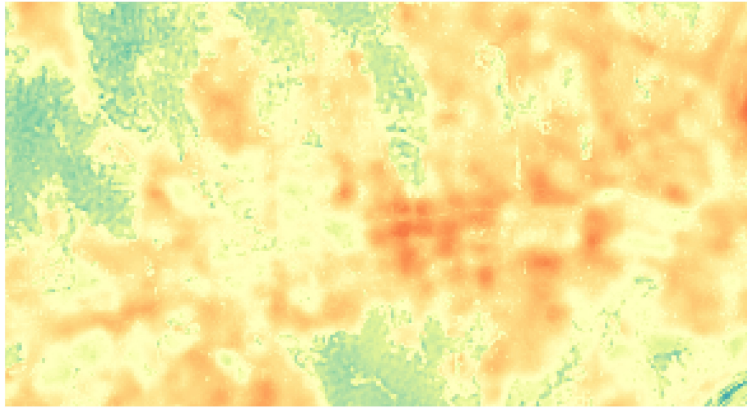


(a) Landsat-8 OLI



(b) Low-resolution BT

[Figure 6.2] Evaluation of results in subset A (Continue)



(c) RTS-NDVI (DisTrad)

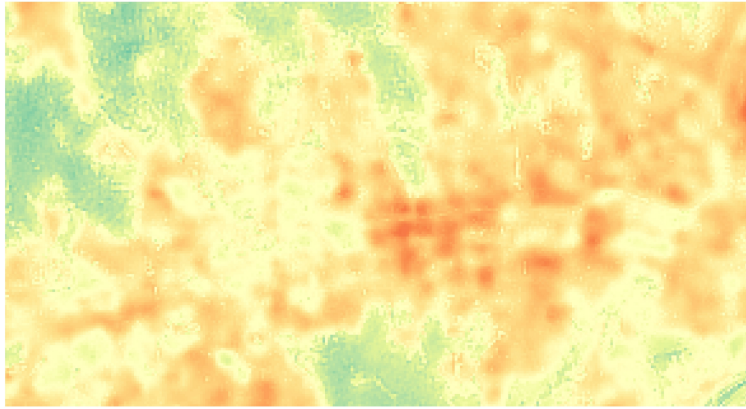


(d) RTS-FVC (TsHARP)



(e) RTS-FUC

[Figure 6.2] Evaluation of results in subset A (Continue)



(f) MRHTS-NDVI

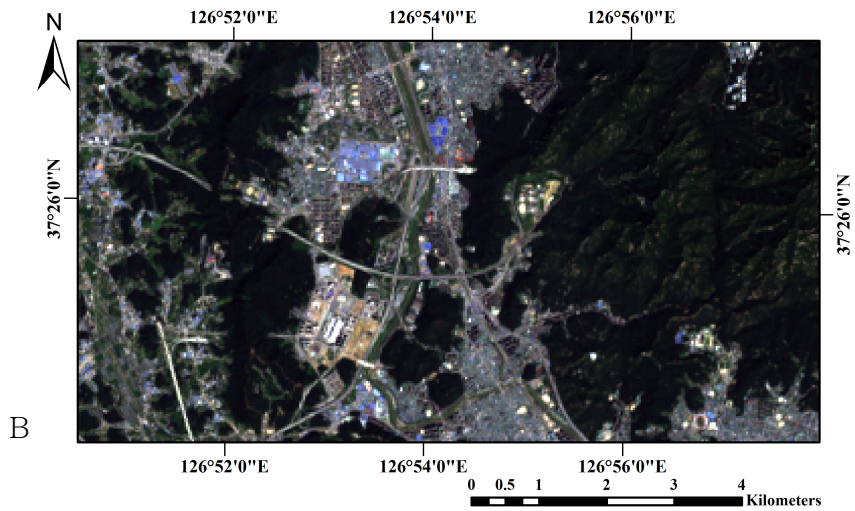


(g) MRHTS-FVC

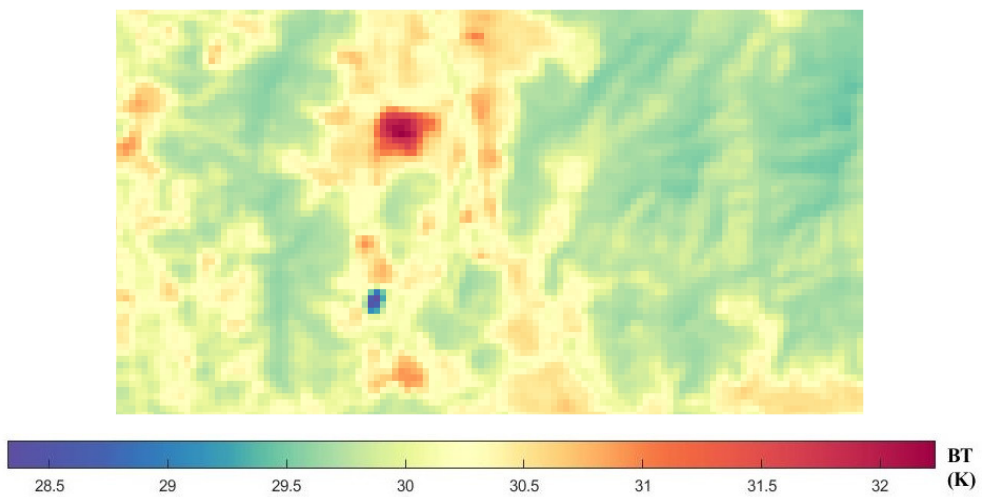


(h) MRHTS-FVC (Proposed)

[Figure 6.2] Evaluation of results in subset A

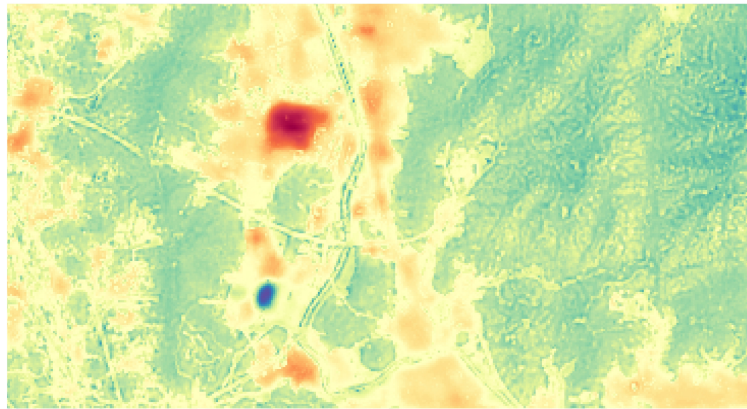


(a) Landsat-8 OLI

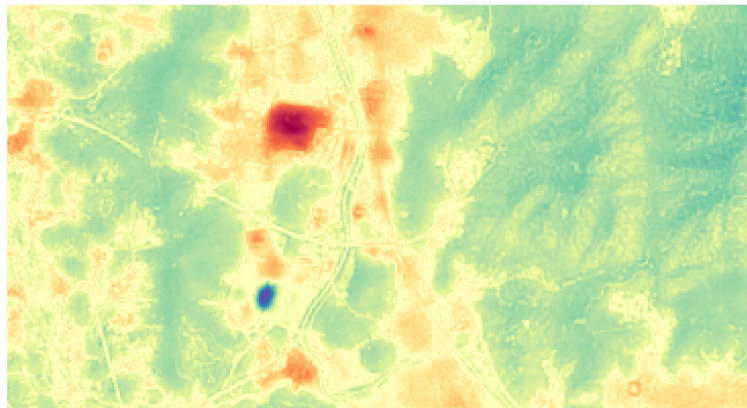


(b) Low-resolution BT

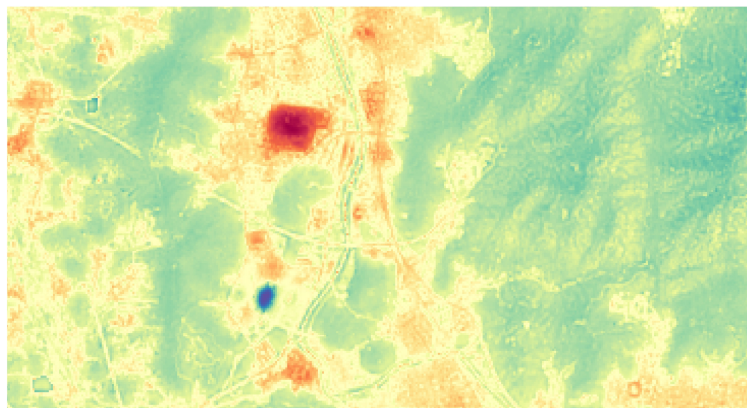
[Figure 6.3] Evaluation of results in subset B (Continue)



(c) RTS-NDVI (DisTrad)

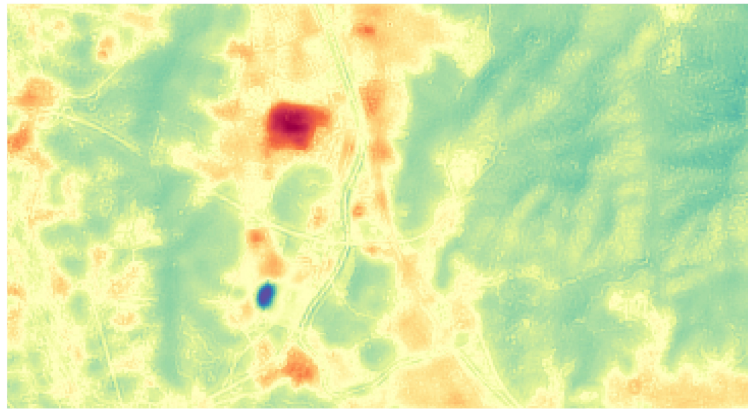


(d) RTS-FVC (TsHARP)

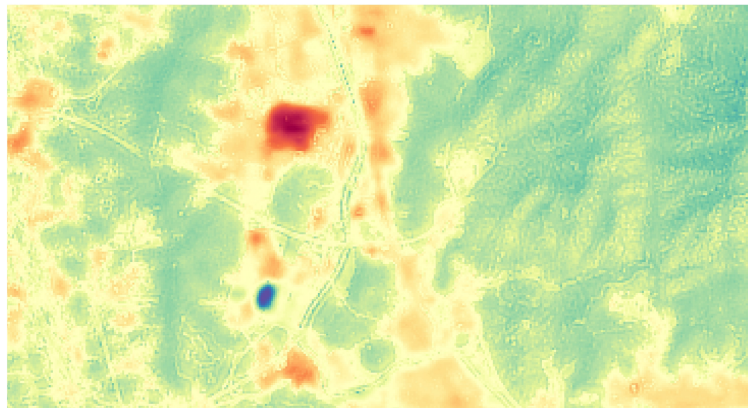


(e) RTS-FVC

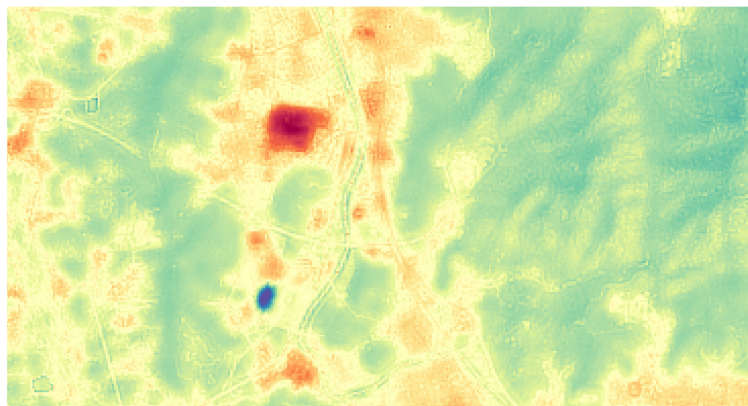
[Figure 6.3] Evaluation of results in subset B (Continue)



(f) MRHTS-NDVI

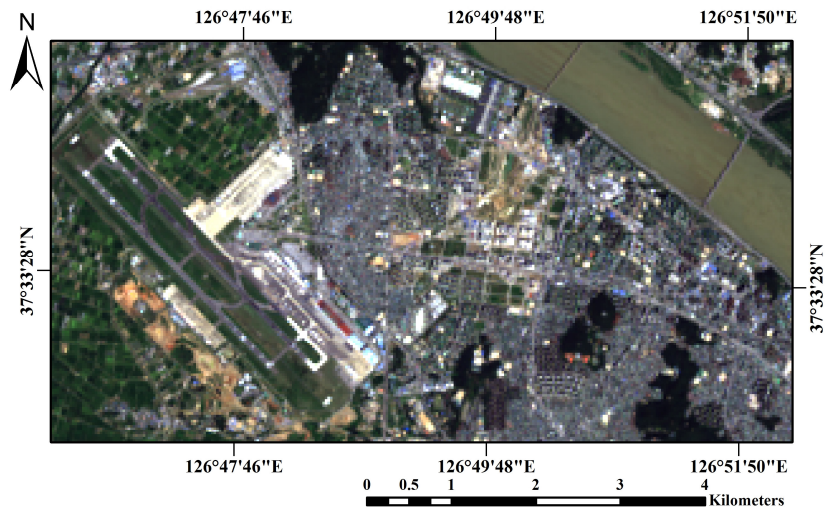


(g) MRHTS-FVC

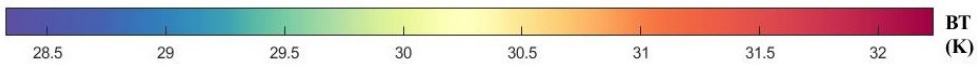
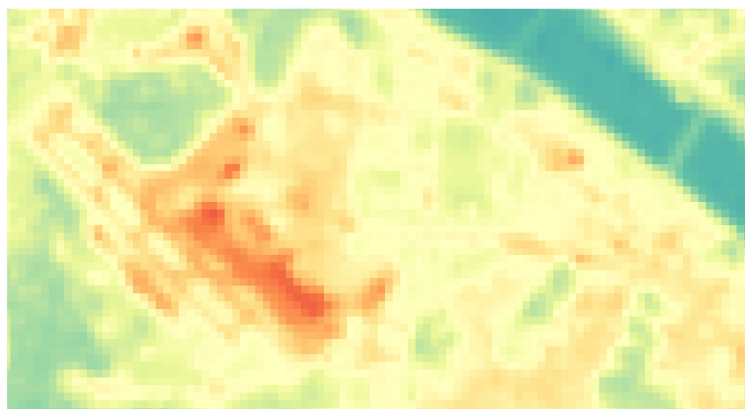


(h) MRHTS-FUC (Proposed)

[Figure 6.3] Evaluation of results in subset B

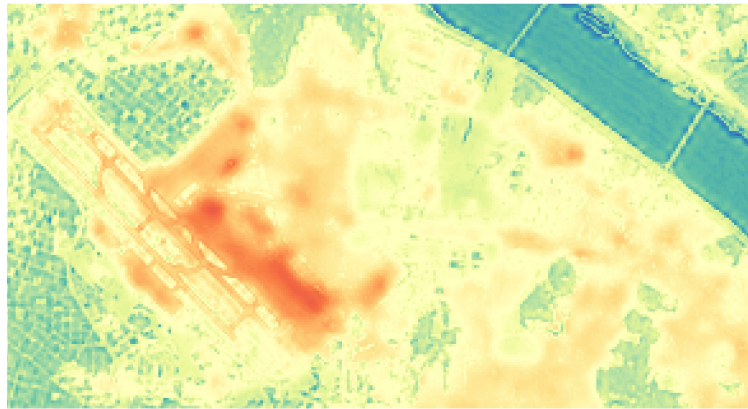


(a) Landsat-8 OLI



(b) Low-resolution BT

[Figure 6.4] Evaluation of results in subset C (Continue)



(c) RTS-NDVI (DisTrad)



(d) RTS-FVC (TsHARP)



(e) RTS-FVC

[Figure 6.4] Evaluation of results in subset C (Continue)



(f) MRHTS-NDVI



(g) MRHTS-FVC



(h) MRHTS-FVC (Proposed)

[Figure 6.4] Evaluation of results in subset C

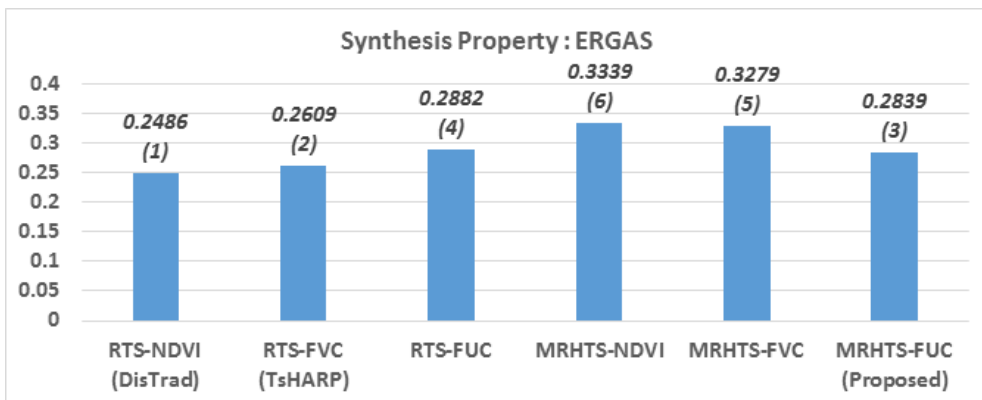
## 6.2 Quantitative Analysis

For quantitative analysis, the spectral preservation of the MRHTS sharpening model and the spatial details by the FUC index were clearly visible. Figures 6.5 and 6.6 present the results of image quality assessment based on the synthesis and consistency properties.

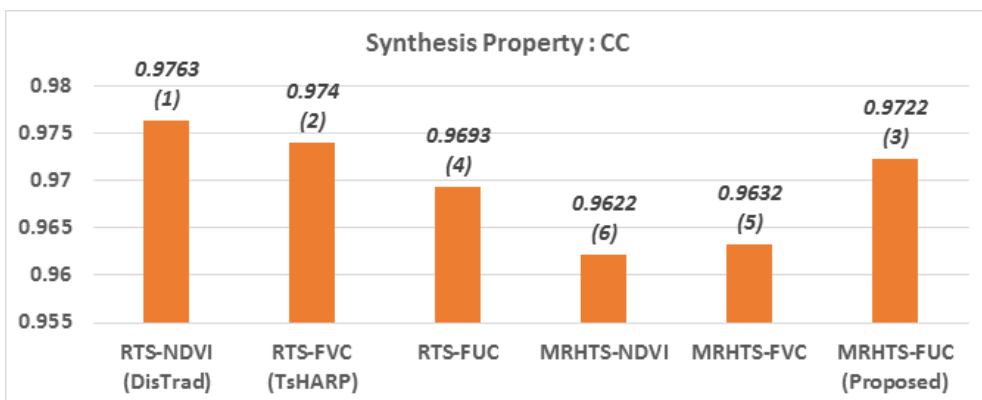
First of all, results based on the synthesis property are presented in Figure 6.5. The values of ERGAS and CC, indicating the preservation of spectral characteristics of the sharpened image, were higher for the RTS-NDVI method, followed by the RTS-FVC and the proposed MRHTS-FUC method. The VI-based RTS methods (RTS-NDVI and RTS-FVC) demonstrated better result than the FUC-based methods (RTS-FUC and MRHTS-FUC) in terms of spectral distortion.

Contrary to ERGAS and CC, the SSIM index, which specifies the preservation of spatial characteristics of the sharpened image, recorded the highest value for the MRHTS-FUC algorithm over the other compared methods. The results based on the synthesis property from the SSIM index were well-reflected in the visual evaluation. In the case of RTS-FUC method ranked the lowest in the SSIM evaluation. This result signified that the result of the RTS-FUC method showing the finest spatial details is over-sharpened, and the MRHTS framework in the FUC index seemed to prevent over-sharpening of spatial details.

This tendency also appears in the UIQI index, which considers the preservation of spatial and spectral characteristics of the sharpened image simultaneously. As a result, the proposed MRHTS-FUC sharpening can reflect the spatial details better than the RTS-NDVI and RTS-FVC methods. Furthermore, when VI-based indices (NDVI and FVC) were used as inputs for the MRHTS framework, the evaluation results for all of the image quality indices were poorer in comparison to the results of the proposed algorithm.

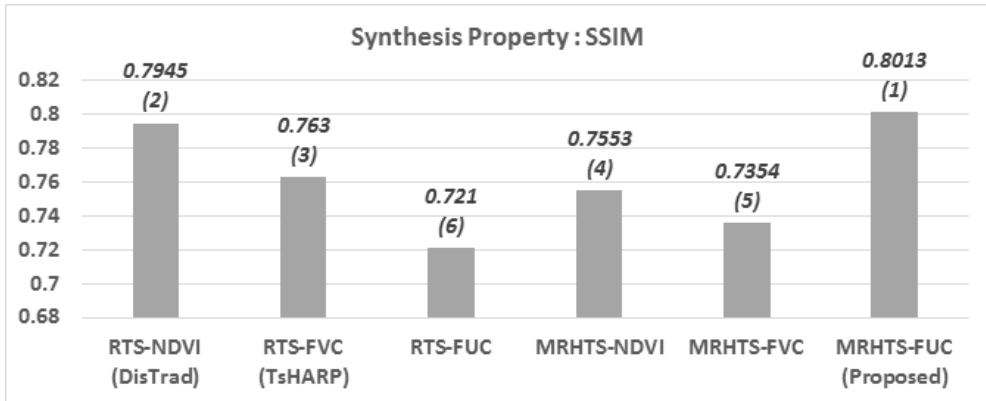


(a)

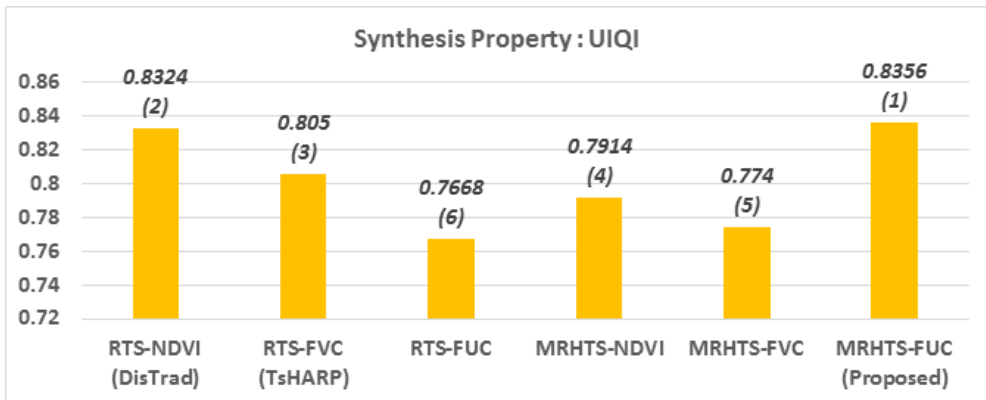


(b)

[Figure 6.5] Result of image quality assessment for synthesis property (Continue)



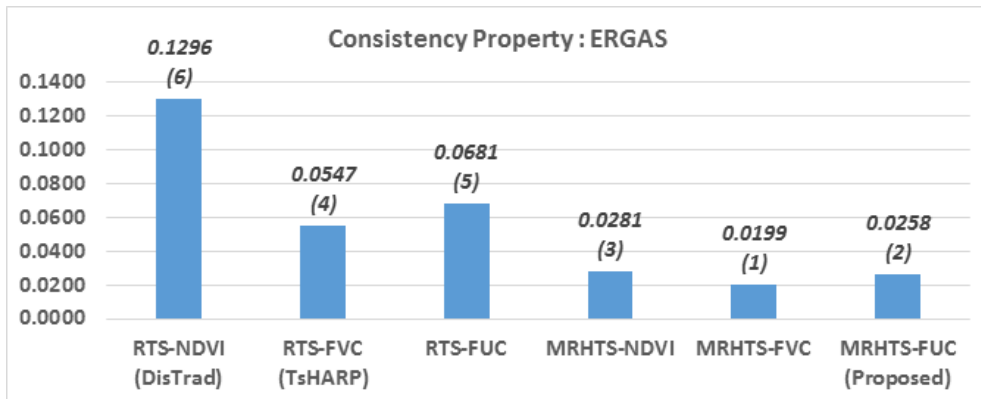
(c)



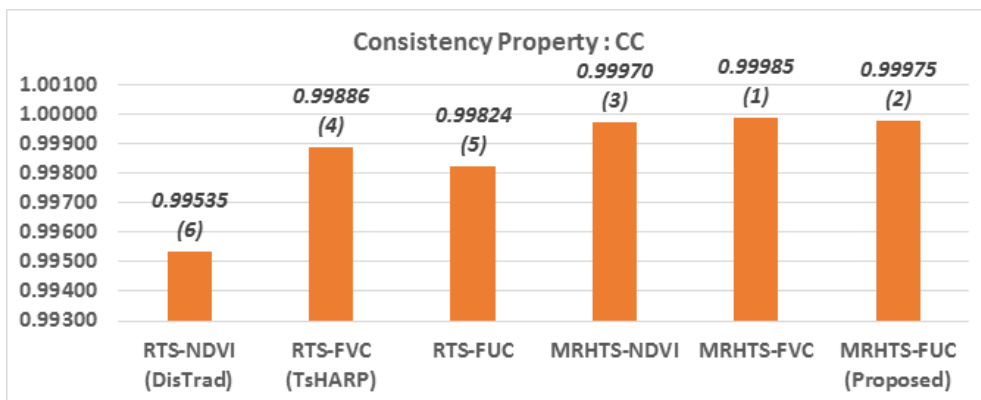
(d)

[Figure 6.5] Result of image quality assessment for synthesis property: (a) ERGAS, (b) CC, (c) SSIM and (d) UIQI, the ranking of each image quality index by algorithms is shown below the value of index..

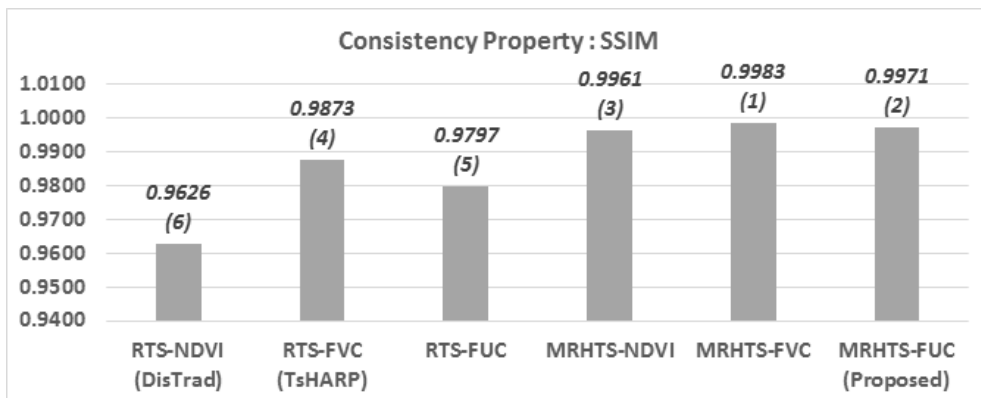
For the consistency property summarized in Figure 6.6, the spectral properties are well-preserved, which is an advantage of the MRHTS framework proposed in this study. The results of the quantitative analysis indicated that the MRHTS framework produced better results for all index in comparison to the RTS framework.



(a)

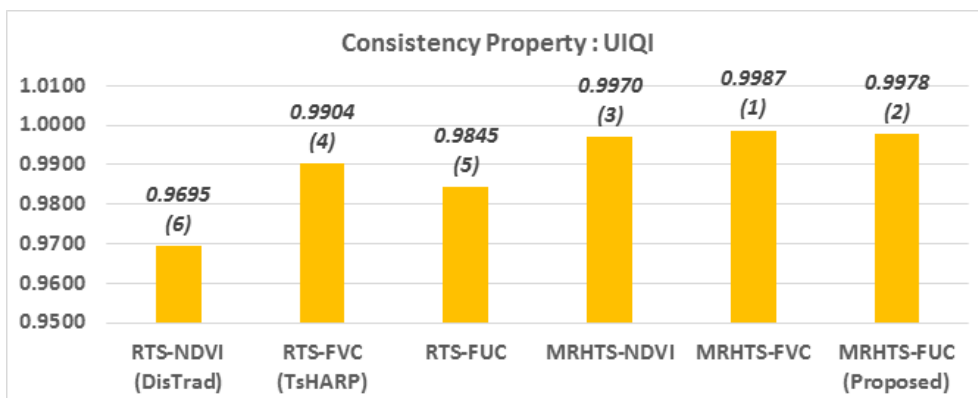


(b)



(c)

[Figure 6.6] Result of image quality assessment for consistency property (Continue)



(d)

[Figure 6.6] Result of image quality assessment for consistency property: (a) ERGAS, (b) CC, (c) SSIM and (d) UIQI, the ranking of each image quality index by algorithms is shown below the value of index.

The two properties of the Wald's protocol are based on the scale invariant assumption of the sharpening method to complement the absence of a reference image, but are not absolute criteria. In addition, an algorithm that works well only for a specific protocol cannot be selected if it satisfies only one of the assumptions. Thus, both the synthesis and consistency properties were needed to be considered collectively. In this regard, VI-based RTS algorithms are not appropriate for thermal sharpening in urban areas. Even though the VI-based RTS algorithms presented the best quality of spectral preservation in the synthesis property, they showed the worst image quality in the consistency property. Likewise, VI-based MRHTS algorithms exhibited acceptable quantitative results for the synthesis property, but the worst image quality assessment for the consistency property. Also, VI-based algorithms (RTS-NDVI,

RTS-FVC, MRHTS-NDVI and MRHTS-FVC) tended to under-sharpen features in urban areas according to visual evaluation in the previous section. In the case of MRHTS-FUC, the algorithm revealed appropriate sharpness through visual analysis, the most effective degree of preservation of spatial features in terms of the synthesis property and effective preservation of spectral features using the MRHTS framework in terms of the consistency property.

In conclusion, the proposed algorithm (MRHTS-FUC) displayed satisfying sharpening results in terms of both sharpness in the urban and vegetation areas from the visual evaluation, as well as acceptable results in both the evaluation protocols. The thermal spatial details of the original BT data were, therefore, preserved in the sharpened result for the proposed algorithm. However, as shown in the visual assessment, the under-sharpening problem of the proposed algorithm in waterbody areas needs to be solved in future work.

## 7. Conclusion

In this study, an improved thermal sharpening algorithm of Landsat-8 TIRS using a novel index was proposed with the integration of fractional urban cover derived from VIIRS DNB NTL imagery for urban areas. Also, the MRHTS sharpening framework was used to prevent spectral distortion of the original TIR data. The suggested FUC index, which is more correlated with BT than the NDVI and FVC, displayed the ability to successfully preserve radiometric information in the form of high temperature components.

The Landsat-8 OLI, TIRS, and VIIRS DNB NTL images of the urban area were used to evaluate the MRHTS-FUC algorithm proposed in this study with comparison to algorithms based on the NDVI and FVC. The experimental results demonstrated that the proposed algorithm sharpened the BT data from 90-m resolution to 30-m resolution, which satisfied image quality assessments in terms of visual and quantitative evaluations.

For the synthesis property, the proposed algorithm yielded better results for UIQI and SSIM, while contrastingly, the algorithm recorded poorer results for ERGAS and CC in comparison to RTS-NDVI and RTS-FVC (Figure 6.5). These results reflect how the proposed algorithm effectively reflects the spatial details of the image from the FUC index. On the other hand, for the consistency property, the MRHTS framework

returned better results than the RTS framework for all image quality indices (Figure 6.6). The quantitative results demonstrate that the proposed algorithm demonstrates better sharpening results with acceptable image quality assessments of both protocols.

In addition, visual analysis (Figures 6.1-4) demonstrated that the proposed algorithm extracted spatial detail in the urban area with effective preservation of spectral features. However, in areas which consist of waterbodies, the under-sharpening trends generated in the results of the proposed algorithm will be improved in further research. The significance of this research is the ability to conduct analysis of urban morphology over land cover and land use level by enhancing the spatial resolution of the temperature image. In other words, the proposed method is expected to improve thermal imagery, which was previously restricted in terms of spatial resolution compared to MS sensors, thereby expanding its practical utilization at a finer scale for future practical applications.

## Bibliography

- Agam, N., Kustas, W. P., Anderson, M. C., Li, F., & Neale, C. M. (2007). A vegetation index based technique for spatial sharpening of thermal imagery. *Remote sensing of environment*, *107*(4), 545–558.
- Allison, R. S., Johnston, J. M., Craig, G., & Jennings, S. (2016). Airborne optical and thermal remote sensing for wildfire detection and monitoring. *Sensors*, *16*(8), 1310.
- Alparone, L., Garzelli, A., & Vivone, G. (2017). Intersensor statistical matching for pansharpening: Theoretical issues and practical solutions. *IEEE Transactions on Geoscience and Remote Sensing*, *55*(8), 4682–4695.
- Banzhaf, E., & Hofer, R. (2008). Monitoring urban structure types as spatial indicators with CIR aerial photographs for a more effective urban environmental management. *IEEE Journal of Selected Topics in Applied Earth Observations and Remote Sensing*, *1*(2), 129–138.
- Bindhu, V., Narasimhan, B., & Sudheer, K. (2013). Development and verification of a non-linear disaggregation method (NL-DisTrad) to downscale MODIS land surface temperature to the spatial scale of Landsat thermal data to estimate evapotranspiration. *Remote sensing of environment*, *135*, 118–129.

- Bisquert, M., Sánchez, J., López-Urrea, R., & Caselles, V. (2016). Estimating high resolution evapotranspiration from disaggregated thermal images. *Remote sensing of environment*, 187, 423–433.
- Blackett, M. (2014). Early analysis of Landsat-8 thermal infrared sensor imagery of volcanic activity. *Remote Sensing*, 6(3), 2282–2295.
- Bonafoni, S. (2016). Downscaling of Landsat and MODIS land surface temperature over the heterogeneous urban area of Milan. *IEEE Journal of Selected Topics in Applied Earth Observations and Remote Sensing*, 9(5), 2019–2027.
- Chander, G., Markham, B. L., & Helder, D. L. (2009). Summary of current radiometric calibration coefficients for Landsat MSS, TM, ETM+, and EO-1 ALI sensors. *Remote sensing of environment*, 113(5), 893–903.
- Chen, X., Li, W., Chen, J., Rao, Y., & Yamaguchi, Y. (2014). A combination of TsHARP and thin plate spline interpolation for spatial sharpening of thermal imagery. *Remote Sensing*, 6(4), 2845–2863.
- Chen, Y., Zhan, W., Quan, J., Zhou, J., Zhu, X., & Sun, H. (2014). Disaggregation of remotely sensed land surface temperature: A generalized paradigm. *IEEE Transactions on Geoscience and Remote Sensing*, 52(9), 5952–5965.

- Cho, K., Kim, Y., & Kim, Y. (2018). Disaggregation of Landsat-8 Thermal Data Using Guided SWIR Imagery on the Scene of a Wildfire. *Remote Sensing*, *10*(1), 105.
- Dominguez, A., Kleissl, J., Luvall, J. C., & Rickman, D. L. (2011). High-resolution urban thermal sharpener (HUTS). *Remote sensing of environment*, *115*(7), 1772–1780.
- Elvidge, C. D., Cinzano, P., Pettit, D., Arvesen, J., Sutton, P., Small, C., Nemani, R., Longcore, T., Rich, C., & Safran, J. (2007). The Nightsat mission concept. *International Journal of Remote Sensing*, *28*(12), 2645–2670.
- Essa, W., Verbeiren, B., van der Kwast, J., Van de Voorde, T., & Batelaan, O. (2012). Evaluation of the DisTrad thermal sharpening methodology for urban areas. *International Journal of Applied Earth Observation and Geoinformation*, *19*, 163–172.
- Felde, G., Anderson, G., Cooley, T., Matthew, M., Berk, A., & Lee, J. (2003). *Analysis of Hyperion data with the FLAASH atmospheric correction algorithm*. Paper presented at the Geoscience and Remote Sensing Symposium, 2003. IGARSS'03. Proceedings. 2003 IEEE International.

- Guo, L. J., & Moore, J. M. (1998). Pixel block intensity modulation: adding spatial detail to TM band 6 thermal imagery. *International Journal of Remote Sensing*, 19(13), 2477–2491.
- Huang, C., Yang, J., & Jiang, P. (2018). Assessing Impacts of Urban Form on Landscape Structure of Urban Green Spaces in China Using Landsat Images Based on Google Earth Engine. *Remote Sensing*, 10(10), 1569.
- Hutengs, C., & Vohland, M. (2016). Downscaling land surface temperatures at regional scales with random forest regression. *Remote sensing of environment*, 178, 127–141.
- Jeganathan, C., Hamm, N., Mukherjee, S., Atkinson, P. M., Raju, P., & Dadhwal, V. (2011). Evaluating a thermal image sharpening model over a mixed agricultural landscape in India. *International Journal of Applied Earth Observation and Geoinformation*, 13(2), 178–191.
- Jia, Y., Huang, Y., Yu, B., Wu, Q., Yu, S., Wu, J., & Wu, J. (2017). Downscaling land surface temperature data by fusing Suomi NPP–VIIRS and landsat–8 TIR data. *Remote Sensing Letters*, 8(12), 1133–1142.

- Jiang, Y., & Weng, Q. (2017). Estimation of hourly and daily evapotranspiration and soil moisture using downscaled LST over various urban surfaces. *GIScience & Remote Sensing*, *54*(1), 95–117.
- Jing, L., & Cheng, Q. (2010). A technique based on non-linear transform and multivariate analysis to merge thermal infrared data and higher-resolution multispectral data. *International Journal of Remote Sensing*, *31*(24), 6459–6471.
- Kalma, J. D., McVicar, T. R., & McCabe, M. F. (2008). Estimating land surface evaporation: A review of methods using remotely sensed surface temperature data. *Surveys in Geophysics*, *29*(4–5), 421–469.
- Kaneda, T., Greenbaum, C., & Patierno, K. (2018). 2018 World Population Data Sheet. *Population Reference Bureau*, *13*, 2018.
- Kolios, S., Georgoulas, G., & Stylios, C. (2013). Achieving downscaling of Meteosat thermal infrared imagery using artificial neural networks. *International Journal of Remote Sensing*, *34*(21), 7706–7722.

- Kustas, W. P., Norman, J. M., Anderson, M. C., & French, A. N. (2003). Estimating subpixel surface temperatures and energy fluxes from the vegetation index–radiometric temperature relationship. *Remote sensing of environment*, *85*(4), 429–440.
- Li, J., Song, C., Cao, L., Zhu, F., Meng, X., & Wu, J. (2011). Impacts of landscape structure on surface urban heat islands: a case study of Shanghai, China. *Remote sensing of environment*, *115*(12), 3249–3263.
- Li, X., Xin, X., Jiao, J., Peng, Z., Zhang, H., Shao, S., & Liu, Q. (2017). Estimating Subpixel Surface Heat Fluxes through Applying Temperature–Sharpening Methods to MODIS Data. *Remote Sensing*, *9*(8), 836.
- Li, X., Zhao, L., Li, D., & Xu, H. (2018). Mapping Urban Extent Using Luojia 1–01 Nighttime Light Imagery. *Sensors*, *18*(11), 3665.
- Liu, J. (2000). Smoothing filter–based intensity modulation: A spectral preserve image fusion technique for improving spatial details. *International Journal of Remote Sensing*, *21*(18), 3461–3472.
- Lu, D., Tian, H., Zhou, G., & Ge, H. (2008). Regional mapping of human settlements in southeastern China with multisensor remotely sensed data. *Remote sensing of environment*, *112*(9), 3668–3679.

- Merlin, O., Duchemin, B., Hagolle, O., Jacob, F., Coudert, B., Chehbouni, G., Dedieu, G., Garatuza, J., & Kerr, Y. (2010). Disaggregation of MODIS surface temperature over an agricultural area using a time series of Formosat-2 images. *Remote sensing of environment*, *114*(11), 2500–2512.
- Moosavi, V., Talebi, A., Mokhtari, M. H., Shamsi, S. R. F., & Niazi, Y. (2015). A wavelet-artificial intelligence fusion approach (WAIFA) for blending Landsat and MODIS surface temperature. *Remote sensing of environment*, *169*, 243–254.
- Mukherjee, S., Joshi, P., & Garg, R. (2014). A comparison of different regression models for downscaling Landsat and MODIS land surface temperature images over heterogeneous landscape. *Advances in Space Research*, *54*(4), 655–669.
- Murphy, S. W., de Souza Filho, C. R., Wright, R., Sabatino, G., & Pabon, R. C. (2016). HOTMAP: Global hot target detection at moderate spatial resolution. *Remote sensing of environment*, *177*, 78–88.

- Olivera–Guerra, L., Mattar, C., Merlin, O., Durán–Alarcón, C., Santamaría–Artigas, A., & Fuster, R. (2017). An operational method for the disaggregation of land surface temperature to estimate actual evapotranspiration in the arid region of Chile. *ISPRS Journal of Photogrammetry and Remote Sensing*, *128*, 170–181.
- Rashed, T., & Jürgens, C. (2010). *Remote sensing of urban and suburban areas* (Vol. 10): Springer Science & Business Media.
- Rodriguez–Galiano, V., Pardo–Igúzquiza, E., Sanchez–Castillo, M., Chica–Olmo, M., & Chica–Rivas, M. (2012). Downscaling Landsat 7 ETM+ thermal imagery using land surface temperature and NDVI images. *International Journal of Applied Earth Observation and Geoinformation*, *18*, 515–527.
- Roy, D. P., Wulder, M., Loveland, T. R., Woodcock, C., Allen, R., Anderson, M., Helder, D., Irons, J., Johnson, D., & Kennedy, R. (2014). Landsat–8: Science and product vision for terrestrial global change research. *Remote sensing of environment*, *145*, 154–172.
- Singh, R. K., Senay, G. B., Velpuri, N. M., Bohms, S., & Verdin, J. P. (2014). On the downscaling of actual evapotranspiration maps based on combination of MODIS and Landsat–based actual evapotranspiration estimates. *Remote Sensing*, *6*(11), 10483–10509.

- Sismanidis, P., Keramitsoglou, I., Bechtel, B., & Kiranoudis, C. T. (2016). Improving the downscaling of diurnal land surface temperatures using the annual cycle parameters as disaggregation kernels. *Remote Sensing*, *9*(1), 23.
- Stathopoulou, M., & Cartalis, C. (2009). Downscaling AVHRR land surface temperatures for improved surface urban heat island intensity estimation. *Remote sensing of environment*, *113*(12), 2592–2605.
- Sun, L., & Schulz, K. (2015). The improvement of land cover classification by thermal remote sensing. *Remote Sensing*, *7*(7), 8368–8390.
- Vivone, G., Alparone, L., Chanussot, J., Dalla Mura, M., Garzelli, A., Licciardi, G. A., Restaino, R., & Wald, L. (2015). A critical comparison among pansharpening algorithms. *IEEE Transactions on Geoscience and Remote Sensing*, *53*(5), 2565–2586.
- Vivone, G., Restaino, R., Dalla Mura, M., Licciardi, G., & Chanussot, J. (2014). Contrast and error-based fusion schemes for multispectral image pansharpening. *IEEE Geoscience and Remote Sensing Letters*, *11*(5), 930–934.
- Wang, Z., Bovik, A. C., Sheikh, H. R., & Simoncelli, E. P. (2004). Image quality assessment: from error visibility to structural similarity. *IEEE Transactions on Image Processing*, *13*(4), 600–612.

- Wang, Z. B., A. C. (2002). A universal image quality index. *IEEE Signal Processing Letters*, 9(3), 81–84.
- Wickop, E., Böhm, P., Eitner, K., & Breuste, J. (1998). Qualitätszielkonzept für Stadtstrukturtypen am Beispiel der Stadt Leipzig. *UFZ Bericht*, 14, 156.
- Yang, G., Pu, R., Zhao, C., Huang, W., & Wang, J. (2011). Estimation of subpixel land surface temperature using an endmember index based technique: A case examination on ASTER and MODIS temperature products over a heterogeneous area. *Remote sensing of environment*, 115(5), 1202–1219.
- Yang, H., Cong, Z., Liu, Z., & Lei, Z. (2010). Estimating sub-pixel temperatures using the triangle algorithm. *International Journal of Remote Sensing*, 31(23), 6047–6060.
- Yang, Y., Cao, C., Pan, X., Li, X., & Zhu, X. (2017). Downscaling Land Surface Temperature in an Arid Area by Using Multiple Remote Sensing Indices with Random Forest Regression. *Remote Sensing*, 9(8), 789.
- Zakšek, K., Hort, M., & Lorenz, E. (2015). Satellite and ground based thermal observation of the 2014 effusive eruption at Stromboli volcano. *Remote Sensing*, 7(12), 17190–17211.

- Zakšek, K., & Oštir, K. (2012). Downscaling land surface temperature for urban heat island diurnal cycle analysis. *Remote sensing of environment*, *117*, 114–124.
- Zhan, W., Chen, Y., Zhou, J., Li, J., & Liu, W. (2011). Sharpening thermal imageries: A generalized theoretical framework from an assimilation perspective. *IEEE Transactions on Geoscience and Remote Sensing*, *49*(2), 773–789.
- Zhan, W., Chen, Y., Zhou, J., Wang, J., Liu, W., Voogt, J., Zhu, X., Quan, J., & Li, J. (2013). Disaggregation of remotely sensed land surface temperature: Literature survey, taxonomy, issues, and caveats. *Remote sensing of environment*, *131*, 119–139.
- Zhan, W., Huang, F., Quan, J., Zhu, X., Gao, L., Zhou, J., & Ju, W. (2016). Disaggregation of remotely sensed land surface temperature: A new dynamic methodology. *Journal of Geophysical Research: Atmospheres*, *121*(18), 10,538–10,554
- Zhang, D., Tang, R., Zhao, W., Tang, B., Wu, H., Shao, K., & Li, Z.-L. (2014). Surface soil water content estimation from thermal remote sensing based on the temporal variation of land surface temperature. *Remote Sensing*, *6*(4), 3170–3187.

# Appendix

## A.1 Determination of coefficient n for the FUC

The proposed FUC index is expressed by the following equation:

$$FUC = \left( \frac{HSI_{\max} - HSI}{HSI_{\max} - HSI_{\min}} \right)^n$$

The coefficient  $n$  is numerically determined by Matlab at the maximum value of the correlation coefficient between FUC and BT. For numerical analysis,  $n$  is determined so that the maximum value of the correlation is obtained by using  $k$  divided by 10000, which has a range from 0 to 1. Figure A.1 indicates the plot between correlation and  $k$ . When the  $k$  value was 3837 ( $n = 0.3837$ ), the maximum value of the correlation was found to be 0.868.

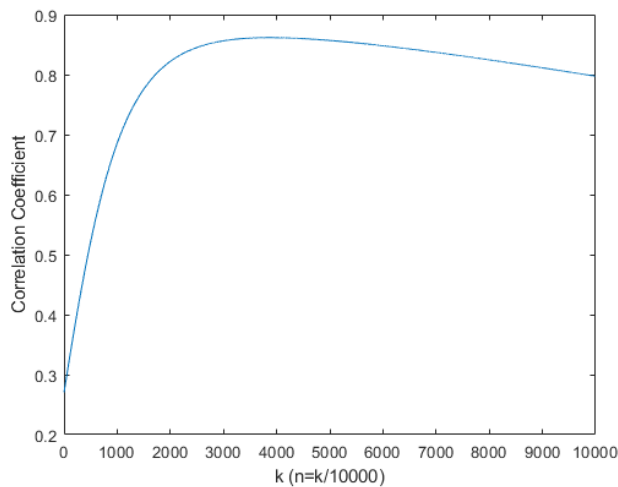


[Figure A.1] Approximated plot between correlation and  $k$

## 국문 초록

원격탐사 플랫폼으로부터 취득된 열 데이터는 전지구적인 생물리학적 현상들을 조사하는 유용한 자료로서 활용되고 있다. 하지만 열적외선 원격탐사 시스템이 가진 공간해상도와 분광해상도의 trade-off 관계로 인해, 다수의 열적외선 원격탐사 센서는 공간해상도 측면에서의 제약이 따른다. 열적외선 원격탐사는 산불, 화산활동, 토지피복분류 및 도심열섬현상 등에 주로 활용되지만 Landsat-8, ASTER (Advanced Spaceborne Thermal Emission and reflection Radiometer) 영상과 같은 중해상도 열적외선 센서는 낮은 공간해상도로 인해 이러한 활용에서의 한계점이 존재한다.

이러한 문제를 개선하기 위해, NDVI (Normalized Different Vegetation Index) 및 FVC (Fractional Vegetation Cover)와 같은 식생지수 기반의 열적외선 공간해상도 향상 알고리즘이 선행연구를 통해 제안되었다. 이 방법들은 식생지역과 같은 균일한 지역에서의 공간적 세밀함을 보존하지만 불균일한 토지피복 패턴이 나타나는 도심지역에서의 공간적 세밀함의 보존에는 한계를 보인다. 이에 본 연구에서는 도심지역 열영상 융합 과정에서 공간적 세밀함의 보존과 동시에 분광적 특성을 보존하기 위해 입력 변수와 모델 선정을 통해 개선된 융합 알고리즘을 제안하였다.

첫째, 열융합 알고리즘의 입력 변수로서 도심 피복 비율 지수 (FUC: Fractional Urban Cover)를 제안하였다. 도심 피복 비율 지수는 VIIRS (Visible Infrared Imaging Radiometer Suite) 센서의 야간시간대 빛 영상 (NTL: Night-Time Light)을 이용하여 생성되었다. 둘째, 분광적 특성의 보존을 위해 최소제곱회귀 분석 및 고주파 변조 분석 기법을 동시

에 이용하는 모델을 제안하였으며, 해당 융합 모델을 변조와 회귀 기반의 하이브리드 열영상 융합 모델 (MRHTS: Modulation and Regression based Hybrid Thermal Sharpening)이라 명명하였다. 최종적으로 본 연구에서 FUC 입력 변수를 이용하여 변조와 회귀 기반의 하이브리드 열영상 융합 모델을 통해 향상된 공간해상도의 열영상을 생성하였다 (MRHTS-FUC).

본 연구에서는 Landsat-8의 다중분광 센서 (OLI: Operational Land Imager), 열적외선 센서 (TIRS: Thermal InfraRed Sensor) 및 VIIRS 야간시간대 빛 영상을 이용하여 제안하는 알고리즘을 적용하였다. 제안된 방법으로 생성된 열영상의 품질 평가를 위해 회귀 기반 열영상 융합 (RTS: Regression based Thermal Sharpening)모델과 식생지수 기반의 입력 변수를 이용하여 생성된 열융합 영상과의 비교평가를 수행하였다. 영상품질평가를 위한 프로토콜은 Synthesis 및 Consistency 특성이 이용되었다.

Synthesis 특성에 대하여, SSIM (Structural SIMilarity)과 UIQI (Universal Image Quality Index)의 값은 제안한 알고리즘 (MRHTS-FUC)에서 가장 높은 값을 나타내었다 (0.8013 및 0.8356). 이러한 결과는 제안하는 MRHTS 열융합 모델이 FUC 입력 변수의 공간적 세밀함을 효과적으로 반영한다는 것을 나타낸다. Consistency 특성에 대해서는 제안하는 MRHTS 열융합 모델이 모든 영상품질평가 지수에 대하여 RTS 열융합 모델보다 더 좋은 결과를 보여주며 융합 영상에서의 분광적 특성의 보존을 잘 나타낸다. 시각적 평가에서도 제안하는 알고리즘의 결과가 도심 피복에서 공간적 세밀함을 가장 잘 표현하였다.

영상품질 평가와 실험 결과, 본 연구에서 제안한 MRHTS-FUC 알고리즘은 분광적 특성 및 공간적 특성을 효과적으로 보존함으로써 도심지역 열적외선 영상의 공간해상도를 향상하였다. Landsat-8 열적외선 영상

의 100-m 공간해상도는 다중분광 센서의 공간해상도인 30-m 수준으로 개선되었다. 향상된 공간해상도의 열영상을 통해 도심 피복 스케일보다 더 세밀한 생활권 및 주거 패턴 기반의 도시 형태학 분석이 가능할 것으로 기대되는 바이다.

**주요어** : Landsat-8 열적외선 센서, 야간시간대 빛 영상, 도심 피복 비율, 변조와 회귀 기반의 하이브리드 열융합 기법, 도심지역

**학 번** : 2017-23626